The Pennsylvania State University

The J. Jeffrey and Ann Marie Fox Graduate School

# URANIUM MÖSSBAUER ARRAY SPECTROSCOPY: A NON-DESTRUCTIVE METHOD FOR DETECTING TRACES OF HIGH ENRICHED URANIUM IN ENVIRONMENTAL SAMPLES

A Thesis in

Nuclear Engineering

by

Matheus R. de Morais



Submitted in Partial Fulfillment

of the Requirements

for the Degree of

Master of Science

May 2025

The thesis of Matheus R. de Morais was reviewed and approved by the following:

Jon Michael Schwantes
Professor of Nuclear Engineering
Thesis Advisor

Federico Scurti
Assistant Professor of Nuclear Engineering

Dipanjan Pan
Huck Chair Professor and Professor of Nuclear Engineering
Graduate Program Chair

# ABSTRACT

This thesis presents the development of a computational model using Python to simulate the Mössbauer effect. This model was used to test and theoretically demonstrate the viability of a new approach, based upon Mössbauer Spectroscopy, to non-destructively detect trace High Enriched Uranium in environmental samples, an approach coined as Uranium Mössbauer Array Spectroscopy (UxMAS). This approach relies on simultaneously measuring $^{234}U$ and $^{238}U$ by Mössbauer Spectroscopy. While $^{235}U$ is not Mossbauer active, $^{235}U$ abundance can be estimated indirectly via the ratio of $^{234}U/^{238}U$. Resonance gammas for the two isotopes are less than 1 keV separated in energy, however, so resolving these gamma lines is key to validating this approach. Model simulations were used here to simulate the simultaneous emission and absorption of resonant gamma rays from excited state $^{234}U$ and $^{238}U$, created by the decay of their radiogenic parents, isotopes $^{238}Pu$ and $^{242}Pu$, respectively. Attempts to simulate the separation of the two gamma lines was approximated by measuring activities across a low (representing $^{234}U$) and a high band region of the gamma energy spectra. The model simulated the effect of varying the speed of the velocity transducer, the resolution of the detector, the isotopic abundance of the sample, and the activities of the sources.

Simulations indicate that detection of traces of HEU are possible with the UxMAS approach, but that detector resolution was a critical design feature of the system. Specifically, employing a detector with a 1% energy resolution was capable of detecting traces of 20% enriched U with a 67% uncertainty. That uncertainty decreased significantly with an increasing level of enrichment. Uranium with an enrichment level of 35%, for instance, could be differentiated from Low Enriched Uranium at High Confidence. Simulations indicated detection could be optimized by adjusting the location of the low and high band regions to coincide with the resonance gamma energy at peak activity for $^{234}U$ and $^{238}U$. Further optimization was created by adjusting the ratio of

the activities of the $^{238}$Pu and $^{242}$Pu sources to favor that of $^{238}$Pu in order to compensate for the large difference in abundance levels between the $^{234}$U and $^{238}$U. Additional advantages may be possible by altering the form of the $^{242}$Pu relative to $^{238}$Pu.

# TABLE OF CONTENTS

# LIST OF FIGURES

# LIST OF TABLES

# ACKNOWLEDGEMENTS

First and foremost, I thank God, who has guided me every step on the way, being the unwavering light on my path. Since the day that I left home country to live alone in a foreign land, His presence has been my source of strength and hope, helping me overcome challenges and reach this point in my life.

I also want to express my heartfelt thanks to my incredible wife, Camila, who has been my rock since the beginning of this journey. Her love, encouragement, and belief in me have been my greatest source of motivation. Even from afar, in another country, she has been my pillar of strength, reminding me why I started this journey and what I am working toward. I am endlessly grateful to have her in my life.

I am deeply grateful to my siblings, André, Leandro and Lilian, and mainly my mother, Eliana, whose sacrifice and unconditional love have made this journey possible. She provided me with everything I needed to be where I am and supported me in every possible way. Her encouragement during difficult times and her unwavering belief in my dreams gave me the courage to continue when I felt like giving up.

I am thankful to my advisor, who gave me the opportunity to work under his guidance and pursue my passion for this field. His support has been invaluable, whether it was through his insightful guidance on research, assistance with literature, advice on academic matters, or even help during times of funding search. His mentorship has been instrumental in my growth, and I am honored to have had the chance to learn from him.

Lastly, I would like to thank my dear friends, Luiz, Ricardo, Jonathan and André Vidal. When I first arrived in the United States and felt the weight of loneliness, their friendship was a beacon of comfort and joy. Also, Jay and Kelley, they all helped me adjust, supported me in

countless ways and made this journey less daunting. I cherish their friendship deeply and hope to stay connected with them, no matter where life takes us.

## Chapter 1

# Introduction

Mössbauer spectroscopy (MS) can detect and characterize the presence of specific isotopes in environmental samples with high selectivity and sensitivity (part per billion levels), non-destructively. In addition to detecting the presence of Mössbauer-active isotopes, MS provides detailed information about the chemical environment surrounding an atom. These characteristics make MS a viable tool for the detection and characterization of anthropogenic Mössbauer active isotopes in the environment. For instance, several Mössbauer active U isotopes can be used to detect indications of nuclear activities in environment samples. Uranium isotopes 234, 236, and 238 are all Mössbauer active, with the former and latter existing as natural isotopes and 236 a biproduct of U that has been in a reactor. So, simply detecting the presence of $^{236}U$ or identifying man-made chemical species like $UO_2F_2$ by MS would indicate the presence of anthropogenic U, although these indicators are not specific to civilian or weapons nuclear activities. To exploit MS as a tool for detecting evidence of nuclear proliferation activities, one must be able to estimate the $^{235}U$ enrichment level, in which the presence of U enriched to 20% or more in isotope 235 would indicate activities associated with a weapons program. While $^{235}U$ is not itself Mössbauer active, the natural abundance of $^{234}U$ is perturbed in a predictable way in the $^{235}U$ enrichment process. Figure 1-1 shows the relationship between the abundance of $^{234}U$ and the enrichment of $^{235}U$ [1,2]. This means, MS could theoretically be used to measure the enrichment of U in environmental samples by simultaneously detecting $^{234}U$, relative to $^{238}U$. Currently, the International Atomic Energy Agency's (IAEA) Network of Analytical Laboratories (NWAL) relies on very time-consuming, destructive, measurements using expensive instrumentation that includes Secondary Ion Mass Spectrometry (SIMS) and Particle based Thermal Ionization Mass Spectrometry (TIMS) to make

these measurements. Developing a MS technique for detecting enriched U particles in environmental samples would provide a means of rapidly screening samples nondestructively prior to SIMS and TIMS measurements.

For many technical reasons discussed later, simultaneously measuring $^{234}U$ and $^{238}U$ by MS is challenging at best and potentially impossible with existing technology. Here, a modeling study is undertaken to ultimately determine the viability of simultaneously measuring $^{234}U$ and $^{238}U$ by MS. If proven viable, the model will be used to develop and optimize a ultra-sensitive, non-destructive, MS method for detecting U proliferation activities in environmental samples.

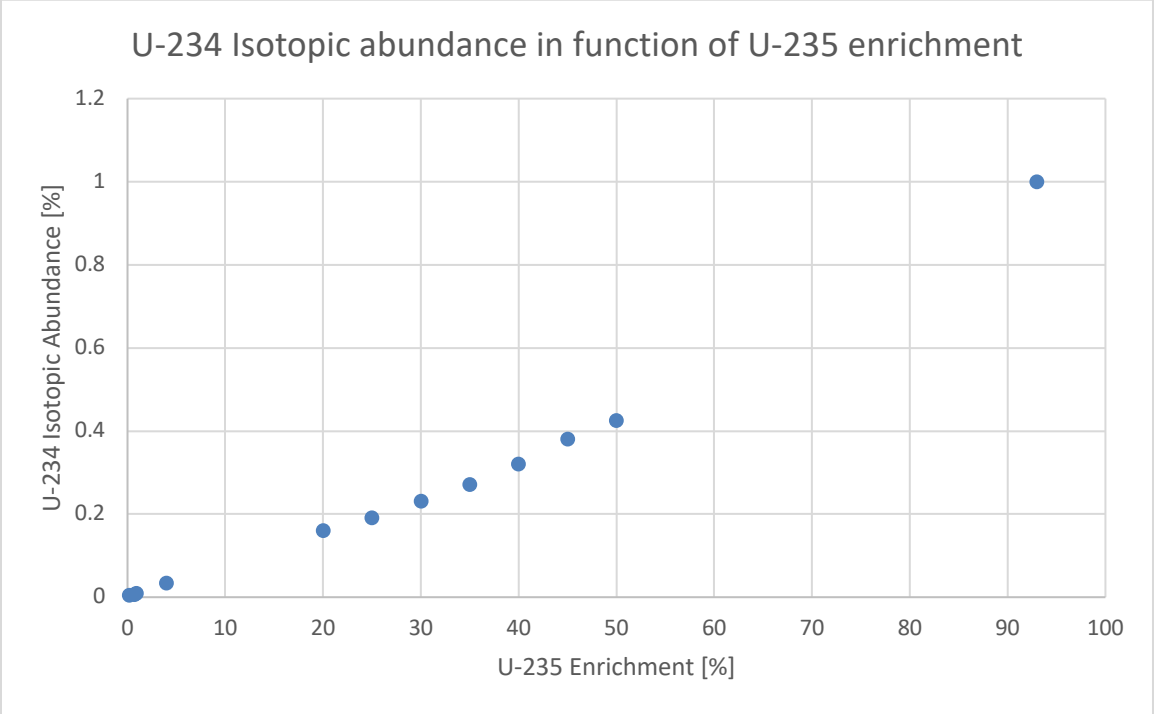


Figure 1-1: Perturbation of $^{234}U$ isotopic abundance as a function of $^{235}U$ enrichment activities

# Chapter 2

# Background

## Mössbauer Spectroscopy

Rudolf Mössbauer in 1957 was the first to observe recoil-free nuclear resonance emission and absorption of gamma rays from the nucleus of an atom bound within a solid matrix. This phenomenon, later termed the Mössbauer Effect, also became the basis for a spectroscopic technique bearing the same name. Mössbauer spectroscopy is a powerful analytical technique utilized in the fields of physics, chemistry, and materials science [3].

The discovery of the Mössbauer effect in 1957 was a remarkable milestone in nuclear physics. Mössbauer observed that certain gamma-ray transition in nuclei could occur without energy loss due to recoil, provided the emitting and absorbing nuclei were part of a crystalline lattice. This observation earned Rudolf the Nobel Prize in Physics in 1961, as it opened new avenues for high-precision measurements in various scientific disciplines [3].

The main feature of the Mössbauer Spectroscopy is the phenomenon of recoil-free gamma-ray emission and absorption. When a gamma ray is emitted or absorbed by a free nucleus, the nucleus experiences a recoil similar to the kickback a gun experiences upon the firing of a bullet from its barrel. Based upon conservation of energy, the product of the recoil energy ($E_R$) and the mass of the nucleus ($M_N$) must equal the product of the gamma ray energy ($E_\gamma$) and the mass of the gamma ray ($M_\gamma$):

$$E_\gamma M_\gamma = E_R M_N \tag{2.1}$$

Rearranging this equation, one can solve for $E_R$ in terms of $M_N$, $M_N$, and $M_\gamma$.

$$E_R = \frac{E_\gamma M_\gamma}{M_N} \tag{2.2}$$

When the nucleus is immobilized within a solid matrix, however, the body experiencing recoil due to the emission of the gamma ray is no longer just the nucleus but the entire solid structure the nucleus is incorporated within. Therefore, equation 1 takes on the new form:

$$E_\gamma M_\gamma = E_R M_S \tag{2.3}$$

Where $M_S$ is the mass of the solid matrix. In this case, $E_R$ is now equal to:

$$E_R = \frac{E_\gamma M_\gamma}{M_S} \approx 0 \tag{2.4}$$

Reducing to 0 as $M_S >> M_\gamma$. This rather unique recoilless gamma emission occurs when $E_\gamma$ is lower than the lowest phonon energy level (usually <150 keV) of the nucleus, any energy loss by vibrational modes. The chemical environments around the emitting and absorbing atoms play a crucial role in the Mossbauer effect, not only allowing for recoilless emission to occur but also affecting the manner in which the emitted gamma ray is absorbed. In other words, the recoilless gamma ray absorption spectrum is characteristic of the chemical environment around the absorbing atom, relative to that of the emitting atom. This phenomenon is the basis for the development of Mossbauer Spectroscopy.

Mössbauer spectroscopy measures the intensity of gamma-ray absorption as a function of the Doppler velocity of the gamma-ray source relative to the absorber. This results in a spectrum characterized by narrow absorption lines corresponding to specific nuclear transitions. Figure 2-1 illustrates the basic components of a Mössbauer spectrometer [4].

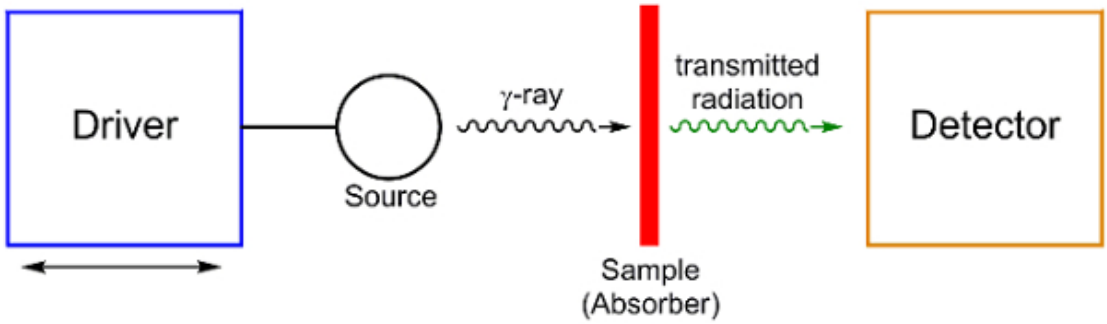


Figure 2-1: Basic instrumental setup for Mössbauer spectroscopy[4]

Mossbauer Spectroscopy has found extensive applications across various fields due to its sensitivity to subtle changes in the nuclear and chemical environments. Applications of Mossbauer Spectroscopy in materials science include studies of electronic, magnetic and structural properties of materials. These studies provide insights into phase transitions, magnetic ordering, and crystallographic structures[5]. Mössbauer spectroscopy has been used to investigate the oxidation states, coordination environments, and chemical bonding of elements, particularly iron and tin Also, it has been studied the possibility to use MS to investigate the hydrogen deposition into Tungsten in Nuclear Fusion reactors to analyze the damaged caused by this severe environment.

The interpretation of Mössbauer spectra involves several key parameters that include Isomer Shifts and Quadrupole and Hyperfine Splitting. Isomer shifts provide information about the

electron density at the nucleus, generally reflecting the oxidation state and chemical environment surrounding the absorbing atom [6]. The Quadrupole splitting arises from the interaction between the nuclear quadrupole moment and the electric field gradient, revealing information about the symmetry and electronic structure of the site [7]. Magnetic Hyperfine Splitting, or Zeeman splitting, is a parameter related to the magnetic interactions at the nuclear site and provides insights into magnetic ordering and local magnetic fields [3].

Mössbauer spectroscopy is a versatile and precise technique that continues to contribute significantly to advancements in various scientific domains. Its ability to probe the atomic-scale environment of nuclei in solids makes it an indispensable tool for researchers. In this thesis, we will explore the application of Mössbauer spectroscopy in the detection of multiples Uranium isotopes, highlighting its role in uncovering new insights and contributing to the broader understanding of this technology and its features.

## The Mössbauer Effect

### Recoil and Line Broadening

When trying to achieve nuclear resonant emission and absorption, two significant obstacles are encountered: recoil energy shift and thermal Doppler shift. Imagine a single atom in a gaseous state, transitioning from an excited state (with energy $E_e$) to its ground state (with energy $E_g$), as shown in Figure 2-2 below:

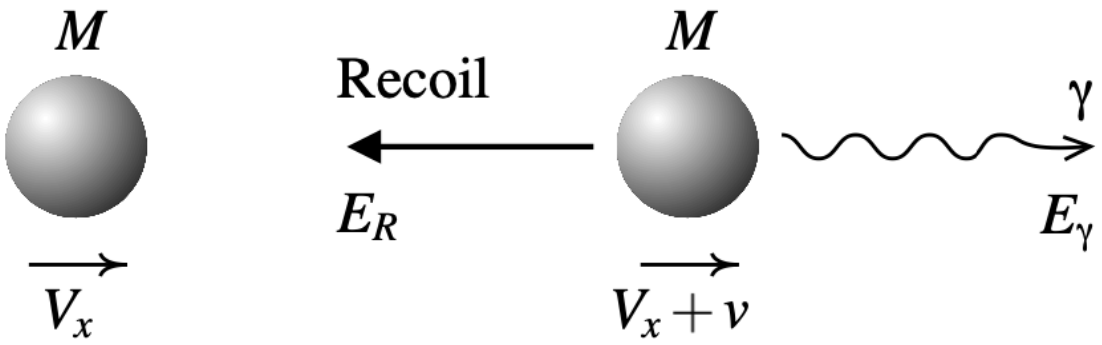


Figure 2-2: The recoil in a free nucleus and the gamma ray emission[8]

When the atom undergoes this transition, it recoils, leading to a recoil kinetic energy ($E_R$) that depends on the mass of the nucleus ($M$) and the energy of the emitted gamma ray ($E_\gamma$). This relationship is given by:

$$E_R = \frac{E_\gamma^2}{2Mc^2} \tag{2.5}$$

Additionally, the energy of the gamma ray is spread into a distribution by the Doppler effect. This Doppler broadening ($E_D$.) depends on the initial velocity of the atom due to its random thermal motion and the recoil from the nucleus. The Doppler broadening can be calculated using:

$$E_D = E_\gamma \sqrt{\frac{2E_k}{Mc^2}} \tag{2.6}$$

Where $E_k$ is the mean kinetic energy of the atom. In this situation, the line broadening due to the Heisenberg Natural Linewidth is negligible because it is extremely small compared to the broadening caused by $E_R$ and $E_D$.

Since the same physics applies to both emission and absorption, a distribution of gamma-ray energies is produced, according to Figure 2-3. However, the overlap between these energies is minimal, making it impractical as a technique [8].

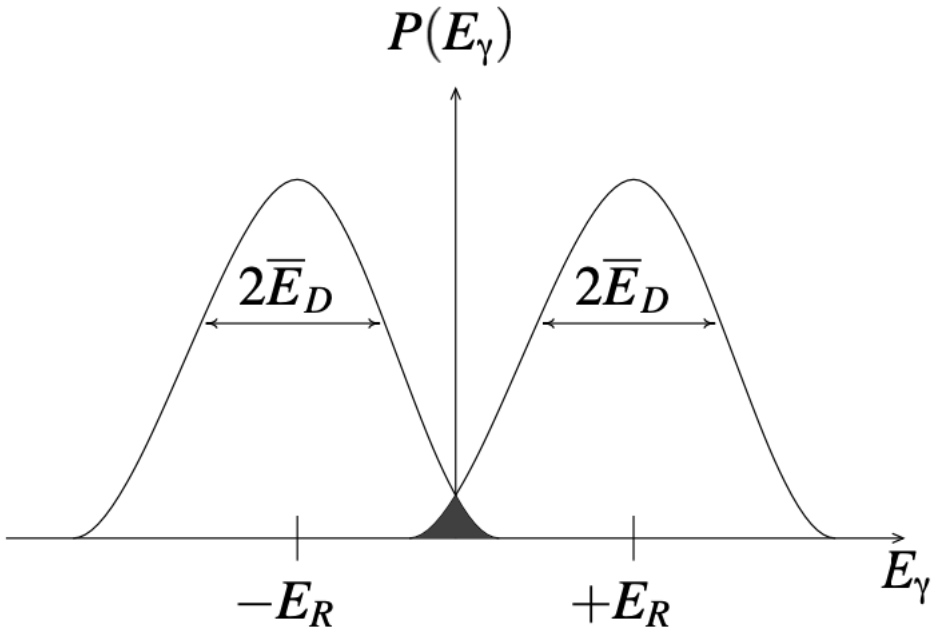


Figure 2-3: Gamma ray distribution for emission and absorption[8]

**Doppler effect**

The Doppler shift refers to the change in frequency caused by the relative motion between a source and an observer. In this case, the frequency of the gamma ray observed by the observer

can be calculated where $f$ is the velocity of the wave, which for our scenario is the speed of light ($c$), $v_r$ is the velocity of the observer, and $v_s$ is the velocity of the source, which is considered positive when the source is moving away from the observer. $f_0$ denotes the initial frequency.

$$f = f_0 \left(\frac{v + v_r}{v + v_s}\right) \tag{2.7}$$

$$f = f_0 \left(\frac{c}{c + v_s}\right) \tag{2.8}$$

When the source moves toward a stationary observer, the observed frequency is higher than the original. Conversely, when the source moves away from the observer, the observed frequencies are lower than the initial wave. The energy of a photon is directly proportional to the product of Planck's constant and the frequency of the electromagnetic radiation. Therefore, as the frequency increases, the corresponding energy also increases, and similarly, when the frequency decreases, the energy decreases as well. [9]

$$E = \frac{hc}{\lambda} = h\nu \tag{2.9}$$

The energy differences between hyperfine states are very small (fractions of an eV), and this variation is achieved by moving the source back and forth relative to the sample in an oscillatory motion, typically at velocities of a few mm/s. The transmittance is then plotted as a function of the source velocity, showing a peak at the velocity corresponding to the resonance energy. In the spectrum below, Figure 2-4, the emission and absorption are both estimated by the Lorentzian distribution [10].

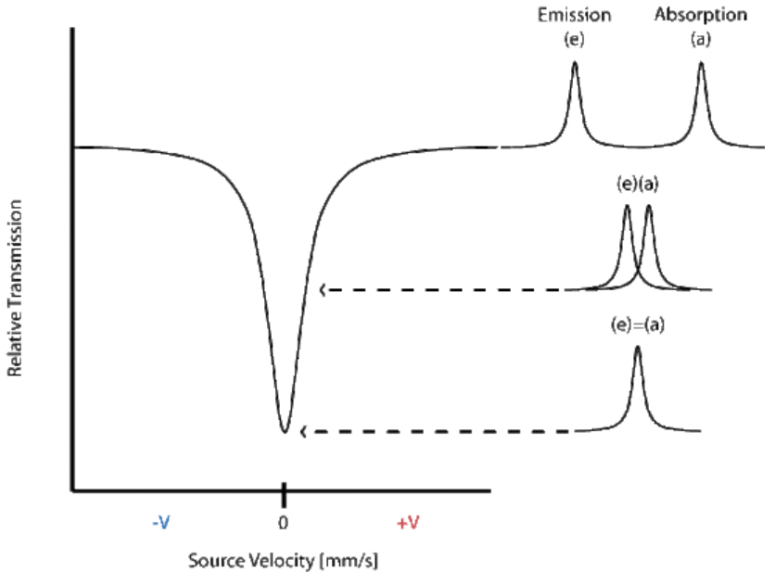


Figure 2-4: Relative transmission spectrum due to the gamma ray emission and absorption[10]

**Recoil-Free Events**

The Mössbauer effect becomes significant when atoms are within a solid lattice or matrix. In such solids, the binding energies are much greater than the recoil energies, meaning the mass that recoils is effectively that of the entire crystal, which is many times greater than that of a single atom. Thus, both the recoil and Doppler effects become negligible.

Despite this, the nucleus within the lattice is still free to vibrate. The recoil energy can transfer into these vibrations as quantized lattice vibrations, or phonons. However, if the recoil energy is less than the energy of the lowest vibrational mode, a recoil-free event occurs. The probability of such an event is governed by the recoil-free factor, $\varphi$, which is calculated as:

$$\varphi = \exp\left(-\frac{E_k\langle x^2\rangle}{\hbar^2 c^2}\right) \tag{2.10}$$

Where $\langle x^2\rangle$ is the mean square vibrational amplitude of the nucleus. The factor $\varphi$ decreases exponentially with the square of the gamma-ray energy, meaning the Mössbauer effect is most detectable in isotopes with low-lying excited states. Optimal detection occurs at temperatures significantly below the Debye Temperature ($\theta_D$) of the material, such as in $^{57}$Fe, where the Mössbauer gamma ray energy is 14.41 keV and $\theta_D$ is 470 K, allowing strong signals to be recorded at room temperature [8].

**Resolution**

In recoil-free events, the Heisenberg Natural Linewidth becomes the limiting factor for gamma ray energy resolution, as it is no longer negligible. For $^{57}$Fe, the energy spread of the gamma rays ($\Gamma_s$) is extremely narrow, leading to a resolution of approximately 1 part in $10^{12}$. This high energy resolution is on the same order as nuclear hyperfine interactions, enabling the Mössbauer effect to probe the electronic environment of a sample in great detail [8].

**Hyperfine Interactions**

Hyperfine interactions in Mössbauer spectroscopy are the interactions between the nuclear states of the Mössbauer isotope and the surrounding electronic and magnetic environment. These interactions provide a wealth of information about the electronic, magnetic, and structural properties of materials. By analyzing the isomer shift, quadrupole splitting, and magnetic hyperfine interactions, researchers can gain insights into the local environment of the nucleus, the nature of

chemical bonds, and the magnetic properties of the material under study. These interactions make Mössbauer spectroscopy a powerful and versatile tool in the fields of chemistry, physics, and materials science [8].

**Isomer shift**

The chemical isomer shift in Mössbauer spectroscopy arises due to the interaction between the nucleus and the surrounding electron cloud. Specifically, it results from a small difference in the electron density at the nucleus when comparing different chemical environments, This shift, in Figure 2-5, can provide insight into the oxidation state, bonding characteristics, and electronic configuration of the atoms withing a material.

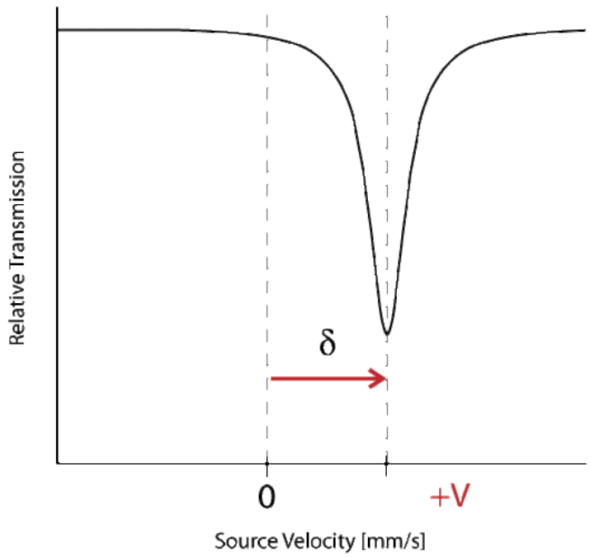


Figure 2-5: Isomer shift example in a Mössbauer spectrum[11]

So, first the nucleus has a finite size and non-uniform charge distribution. During a gamma-ray transition, the radius of the nucleus changes slightly, leading to a small change in the electrostatic potential energy between the nucleus and the surrounding electron cloud.

Then, the electron density at the nucleus, particularly the s-electrons (which have a non-zero probability of being found inside the nucleus), influences the energy levels of the nucleus. Variation in the electron density between different chemical environments cause a shift in the gamma-ray energy, leading to the observed isomer shift.

Also, the shift is sensitive to changes in the oxidation state, coordination number, and the nature of chemical bonds (covalent, ionic, etc.). For example, in iron compounds, the isomer shift can differentiate between $Fe^{2+}$ and $Fe^{3+}$ oxidation states [11].

The isomer shift can be expressed by the following equation:

$$\delta = \frac{2\pi Z e^2}{5}\left(\frac{R_1^2 - R_2^2}{R_2^2}\right)[\rho_s(0) - \rho_r(0)] \tag{2.11}$$

Where the $Z$ is the atomic number, $e$ is the elementary charge, $R_1$ and $R_2$ are the nuclear charge radii in the excited and ground states, respectively, $\rho_s(0)$ is the s-electron density at the nucleus in the sample and $\rho_r(0)$ is the s-electron density at the nucleus in the reference.

The equation (2.11) demonstrates that the isomer shift depends on the difference in s-electron density between the sample and the reference, as well as on the change in nuclear charge radius between the ground and excited states. So, if the isomer shift is positive it means that the electron density at the nucleus in the sample is lower than in the reference. This is often seen in situations where the atom is in a higher oxidation state or when it is more electropositive. However, if the isomer shift is negative this indicates that the electron density at the nucleus in the sample is

higher than in the reference. This may occur when the atom is in a lower oxidation state or when it has more covalent character.

Basically, in iron Mossbauer Spectroscopy ($^{57}Fe$), the isomer shift is commonly measured using a reference absorber, often metallic iron (α-Fe), the isomer shift values can be used to distinguish between $Fe^{2+}$ and $Fe^{3+}$ ions, which have different electrons densities at the nucleus due to their differing oxidation states. For instance, $Fe^{2+}$ (high spin) typically has a larger electron density at the nucleus compared to $Fe^{3+}$, leading to a more negative isomer shift relative to α-Fe, and $Fe^{3+}$ (high spin) shows a smaller or positive isomer shift.

In summary, the chemical isomer shift is a powerful tool in Mössbauer spectroscopy, providing information on the electron density around the nucleus and the chemical environment of the atom. The shift arises from changes in the electrostatic interaction between the nucleus and the surrounding s-electrons during a gamma-ray transition. By analyzing the isomer shift, one can infer details about the oxidation state bonding, and coordination environment of the atom being studied [12]. This data can also be utilized to quantitatively evaluate the electron-withdrawing strength of electronegative substituent groups, as well as the extent of π-bonding and back-donation from metal atoms to ligands in coordination complexes [13].

**Quadrupole Splitting**

The principles discussed so far assume a spherical nuclear charge distribution. However, nuclear states with spin $I > 1/2$ have non-spherical charge distributions, characterized by a nuclear quadrupole moment. When this nuclear quadrupole moment interacts with an asymmetric electric field (such as that created by a non-symmetrical arrangement of electronic charges or ligands), it aligns either along or against the electric field gradient, resulting in the splitting of the nuclear energy levels, represented in the Figure 2-6 below: [14]

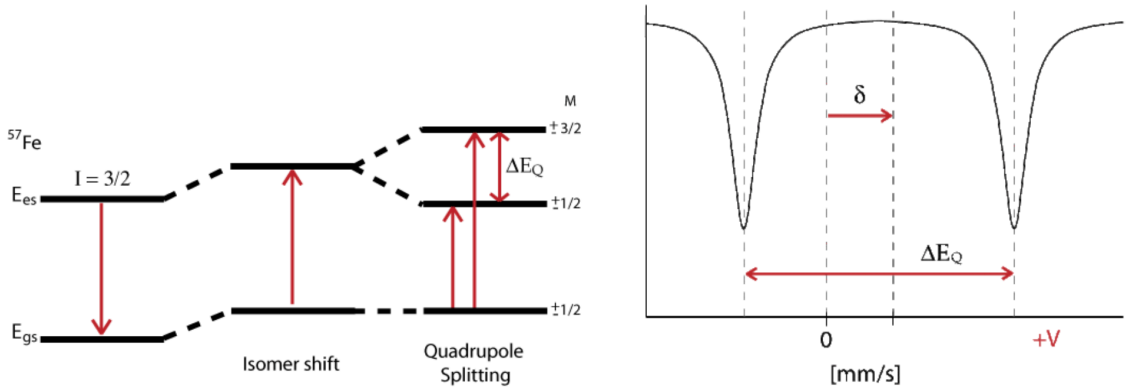


Figure 2-6: Quadrupole splitting example in a Mössbauer spectrum[14]

For instance, in the case of $^{57}$Fe, the excited state ($I = 3/2$) splits into two excited states, producing a two-line spectrum. The Mössbauer quadrupole splitting (Δ) thus provides information about the symmetry of the site occupied by the Mössbauer atom and the electric field gradient at the nucleus. This parameter is highly sensitive, making it effective for detecting slight deviations from ideal symmetry and for determining the energy differences between various orbital states [15]. Quadrupole splitting also yields insights into the electron populations of p- and d-orbitals, isomerization processes, short-lived reaction intermediates, semiconductors, and defects in solid-state materials. This makes it valuable in a wide range of scientific research areas [16].

The quadrupole splitting is proportional to principal component of the electric field gradient tensor, thus:

$$\Delta = \frac{1}{2} e^2 q Q \left(1 + \frac{\eta^2}{3}\right)^{1/2} \tag{2.12}$$

Where, $Q$ is the nuclear quadrupole moment, $e$ is the charge on a proton, $-e^2q$ is the z-component of the electric field gradient tensor ($V_{zz}$) and $\eta$ is the asymmetry parameter equivalent to [8]:

$$\eta = \frac{V_{xx} - V_{yy}}{V_{zz}} \tag{2.13}$$

The electric field gradient consists of contributions from the valence electrons and the charge distribution within the surrounding crystal lattice, as follows:

$$q = (1 - \gamma_\infty)q_{latt} + (1 - R)q_{val} \tag{2.14}$$

Where $\gamma_\infty$ and $R$ are the Sternheimer factor [17], and $q_{latt}$ and $q_{val}$ are the contributions from the crystal lattice and the valence electrons, respectively [18,19].

**Magnetic Hyperfine Splitting**

When a nucleus is exposed to a magnetic field, a magnetic dipole interaction occurs between any nuclear magnetic moment and the magnetic field. This interaction lifts the degeneracy of a nuclear state with an angular momentum quantum number $\boldsymbol{I > 0}$, resulting in the splitting of the state into $\boldsymbol{2I + 1}$ substates. For example, in the case of $^{57}$Fe, the ground state with $\boldsymbol{I = 1/2}$ splits into two substates, while the excited state with $\boldsymbol{I = 3/2}$ splits into four substates. The $\boldsymbol{\Delta m_I = 0, \pm 1}$ selection rule, which governs the Mössbauer gamma-ray transitions, allows six possible transitions, leading to a Mössbauer spectrum characterized by six absorption lines, as illustrated in Figure 2-7 below [20].

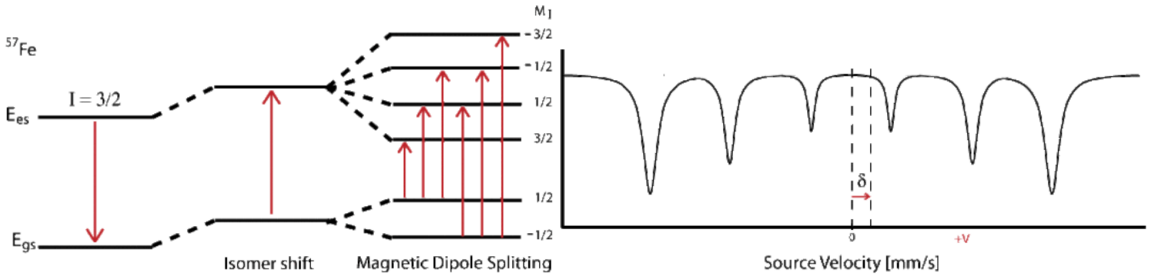


Figure 2-7: Zeeman splitting example in a Mössbauer spectrum[20]

Since the separation of these spectral lines is directly proportional to the magnetic field experienced by the nucleus, Mössbauer spectroscopy serves as an effective tool for measuring this field. The transition probabilities between the nuclear substates influence the intensities of the lines in the Mössbauer spectrum, providing information on the relative orientation of the magnetic field at the nucleus and the direction of the gamma-ray beam [21].

The Hamiltonian for the magnetic dipole interaction is given by:

$$\mathcal{H} = -\boldsymbol{\mu} \cdot \boldsymbol{H} = -g\mu_N \boldsymbol{I} \cdot \boldsymbol{H} \tag{2.15}$$

Where $\mu$ is the nuclear magnetic moment, $g$ is the nuclear g-factor, $\mu_N$ is the nuclear magneton, $I$ is the nuclear spin, and $H$ is the magnetic field at the nucleus. So the corresponding energy eigenvalues are:

$$E_M = -g\mu_N H m_I \tag{2.16}$$

Where $m_I$ represents the magnetic quantum number. The magnetic field splits the nuclear level into equidistant non-degenerate substates, resulting in a spectrum where the magnitude of splitting is proportional to the magnetic field experienced by the nucleus [8].

The total magnetic field experienced by the nucleus is the vector sum of the magnetic hyperfine field and any externally applied magnetic field. The magnetic hyperfine field arises from the unpaired electron spins within the atom and is therefore dependent on the atom's oxidation and spin state. A key aspect of the magnetic hyperfine field is that it is only influenced by unpaired electrons, either directly or indirectly [22].

This interaction is relatively straightforward compared to isomer shift or quadrupole splitting, where contributions may arise from all electrons within the atom, as well as those in the surrounding molecule and lattice [23].

Magnetic hyperfine fields are typically observed in the Mössbauer spectra of magnetically ordered systems, or in paramagnetic systems when the electron spin relaxation times are sufficiently long. Relaxation processes, where electronic spins change direction over characteristic timescales, play an important role in defining the relationship between a magnetic system and its Mössbauer spectra [24].

The ability to apply external magnetic fields offers an additional investigative tool when studying systems with magnetic hyperfine splitting. In such cases, the total magnetic field at the nucleus results from the vector sum of both the hyperfine and external fields, and changes in the spectral line splitting due to the external field can greatly aid in interpreting the spectrum. Among the three Mössbauer hyperfine interactions, the magnetic hyperfine interaction is unique in that it can be readily modified by an external variable.

When magnetic and quadrupole splitting occur together, the Mössbauer spectrum can become more complex, with the observed spectrum being heavily influenced by the relative magnitudes and orientations of these interactions. Applying a magnetic field to a system with no unpaired spins, which therefore lacks a magnetic hyperfine interaction, introduces magnetic splitting alongside quadrupole splitting, providing insights into the geometry of the electric field gradient at the nucleus.

Data from magnetically split Mössbauer spectra can be used to explore magnetic ordering and structure in magnetically ordered systems, understand the nature of magnetic interactions,

determine the magnetic moment of specific atoms, and reveal details of the electronic structure that influence the magnetic hyperfine field at the Mössbauer nucleus [25].

**Mossbauer Spectroscopy in Actinides**

In the periodic table, the elements from $^{89}$Ac to $^{103}$Lr are known as Actinides, their electronic structure cannot be treated in a simple manner. The first half of the series (up to Am with its half-filled 5f shell) exhibits a considerably peculiar electronic behavior [26]. In the Actinides, there is magnetism in all its several forms: from strongly localized (i.e. 4f-like) to totally itinerant (i.e. 3d-like) [27-30].

Curiously, there is a notable resemblance in the nuclear structure of actinides and the heavier lanthanides (beyond Sm). Both groups are situated in regions characterized by strong nuclear deformation, where collective excitations of nuclear matter occur at relatively low energies. A typical feature of these nuclei is the rotational $2^+$ to $0^+$ $E_2$ transitions is around 45 keV. However, the half-life of the excited state is relatively short, approximately 0.2 ns, which unfortunately limits resolution significantly [26]. It is possible to find detailed properties about the MS in actinides in the Appendix A.

**Source and sample**

It is possible to measure Mossbauer spectra for three uranium isotopes using radioactive decay form plutonium parents. The alpha decay of $^{238}$Pu, $^{240}$Pu and $^{242}$Pu leads to the excitation of the 2+ rotational states in $^{234}$U, $^{236}$U and $^{238}$U, respectively [31].

The resonance gamma-ray has been obtained by the alpha decay of the plutonium, for which the decay schemes of $^{242}$Pu, $^{240}$Pu and $^{238}$Pu are shown in Figure 2-8. All these decay schemes are very similar and some of their nuclear properties are compared in Table 2-1. In all cases, the $2^+$ level is fed by about 25% of the decays with the remainder going to the ground state. Higher levels are largely unpopulated, leading to very clean gamma-ray spectra. Unfortunately, the conversion coefficients for all three $0^+$ to $2^+$ ($E_2$ transitions are very large, according to Table 2-1, and the gamma-ray intensities from the sources are noticeably reduced [32]. In the Appendix A, a table containing the Mössbauer transition in Actinide Isotopes can show more details about some parameters that should be considered in some calculations.

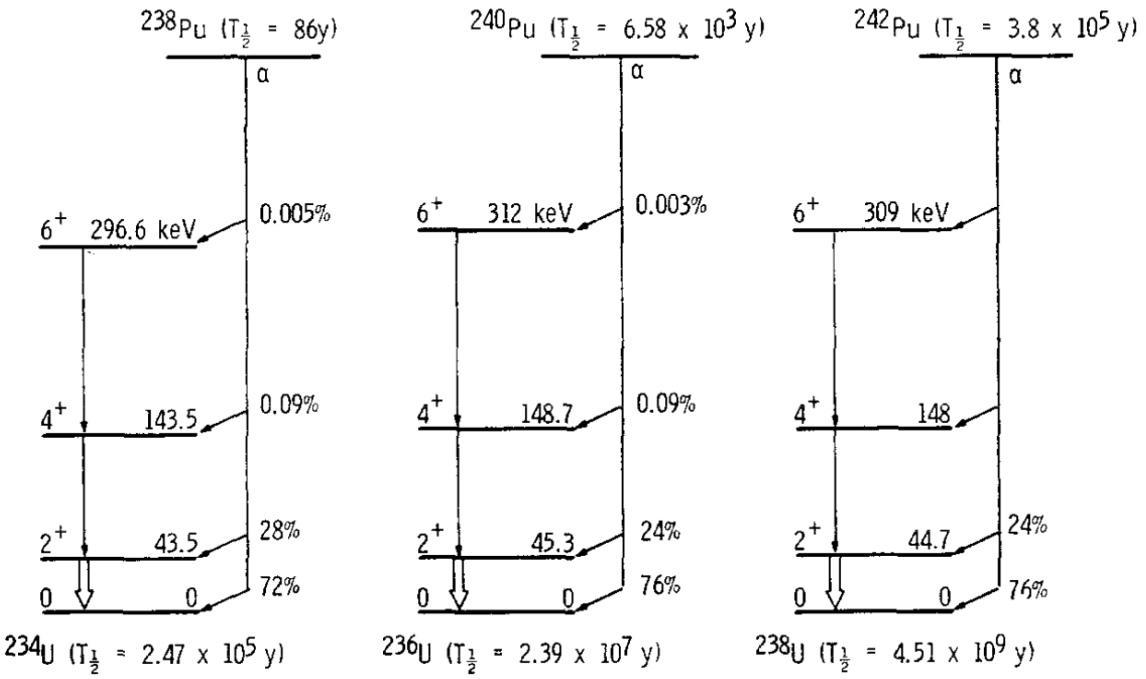


Figure 2-8: Three plutonium isotopes decay to uranium [32]

Table 2-1: Nuclear properties of uranium and their corresponding Plutonium parent [32]

| Isotope | $2^+$ level energy [keV] | $2^+$ level lifetime [ns] | Total conversion coefficient | Source | Source lifetime [y] | Specific Activity [mCi/mg] |
|---|---|---|---|---|---|---|
| $^{234}$U | 43.5 | 0.27 | 780±55 | $^{238}$Pu | 86 | 14.6 |
| $^{236}$U | 45.3 | 0.23 | 607±29 | $^{240}$Pu | $6.58\times10^{3}$ | 0.24 |
| $^{238}$U | 44.7 | 0.23 | 660±30 | $^{242}$Pu | $3.80\times10^{5}$ | $3.9\times10^{-3}$ |

In all three isotopes, the rotational $E_2$ transition is observed around 45 keV, resulting similar Mössbauer properties. The sources are derived from Pu isotopes, which decay by alpha emission.

The key distinction lies in the half-life of the parent isotope. Geometrical constraints limit the allowable source area, while its depth is restricted by photoelectric absorption resonant gamma rays. In all three instances, the gamma activity is reduced due to the high conversion coefficient, but $^{238}$Pu is significantly more potent as a source, being roughly 1000 times stronger than $^{242}$Pu [26]. Regarding the source, however, according to [33] the abundance of isotope $^{234}$U is low (isotopic abundance 0.0057%). Another important aspect of this technique is that the Mössbauer spectrum is only sensitive to the interaction at the resonant nuclei, this way, some impurities and defects will not interfere in the measurement [34].

**Temperature**

The temperature dependence of hyperfine effects is often of interest. If a high-quality source with a large recoil-free fraction at room temperature is available, it may only be necessary to cool the stationary absorber. Otherwise, both the source and absorber may need to be cooled, with one of them also being in motion. Employing standard cryogenic techniques using commercially available vacuum cryostats, MS can be accomplished in the temperature range of 4.2 K to 300 K. Two key considerations specific to Mössbauer spectroscopy at low temperatures include avoiding vibrations inside the cryostat and ensuring a clear path for the gamma-rays from the source to the sample being studied. The vibration issue can be addressed through careful design. Cooling both the vibrating source and the absorber typically requires enclosing the entire transducer unit within the vacuum space.

In Actinide Mössbauer spectroscopy, both the source and the sample must be cooled due to alpha decay. According to [35], the source was cooled to 4.2 K during experiments to achieve better resolution in the spectrum. Also, by [36] is discussed that handling Mössbauer sources and absorbers at cryogenic temperatures to optimize measurements and reduce thermal vibrations. So,

their suggestion is cooling to 4 K to improve the efficiency and resolution of MS experiments, particularly by reducing thermal effects and maximizing the recoil-free fraction of gamma events.

**Velocity transducer**

Moving an object at a constant velocity with high precision and stability, especially when limited by a small range of motion and the need for repetitive motion, presents a significant challenge in applied mechanics. Several types of constant-velocity spectrometers have been developed, which can be categorized into eight distinct groups.

The key advantages of a constant-velocity spectrometer include the ability to investigate a narrow velocity range that is not centered on zero velocity and the direct calibration of the instrument in absolute velocity terms. However, building a precise constant-velocity instrument is both time-consuming and costly, requiring extensive machining and development.

There are also numerous drawbacks. Operating such an instrument manually is labor-intensive unless it is fully automated, which significantly increases the cost. Achieving the necessary precision for linear motion requires highly accurate machining of cams and lead screws, which are prone to mechanical wear and vibration. The velocity range is typically limited to 0.1–10 mm/s, though advanced transducers can extend this range to over 600 mm/s or as low as 0.01 mm/s. Additionally, cam and lead screw systems need a complex automatic reversing mechanism, which discards counts during the velocity change at the end of each cycle.

Moreover, if the source has a short half-life relative to the experiment's duration, gamma emission rates must be corrected for their natural decline over time. These limitations have hindered further advancements in constant-velocity spectrometers, with one of the few recent innovations being an instrument that takes measurements at multiple pre-programmed velocities via punched

tape [37]. Nowadays, most studies rely on repetitive velocity-scan systems, where the central shaft, often rigidly attached to the Mössbauer source, executes precise periodic motion [12]. The actinides are characterized by wide resonances and complex hyperfine splitting that results in the need to conduct MS at relatively high transducer speeds of 150 mm $s^{-1}$ or more. This often results in the need to measure transducer speeds in real time for increased accuracy using a laser interferometer.

**Detection System**

Three conventional detection systems are commonly used in Mössbauer spectroscopy. The scintillation-crystal detector is often employed for gamma rays in the 50-100 keV energy range, with the NaI(Tl) scintillator being a typical example. While scintillators offer high efficiency, their resolution worsens as the energy of the gamma photons decreases, as illustrated in Figure 2-9. These detectors can only be effectively used for very low-energy gamma rays if the background radiation is minimal and there are no interfering X-ray or gamma-ray lines near the Mössbauer transition energy.

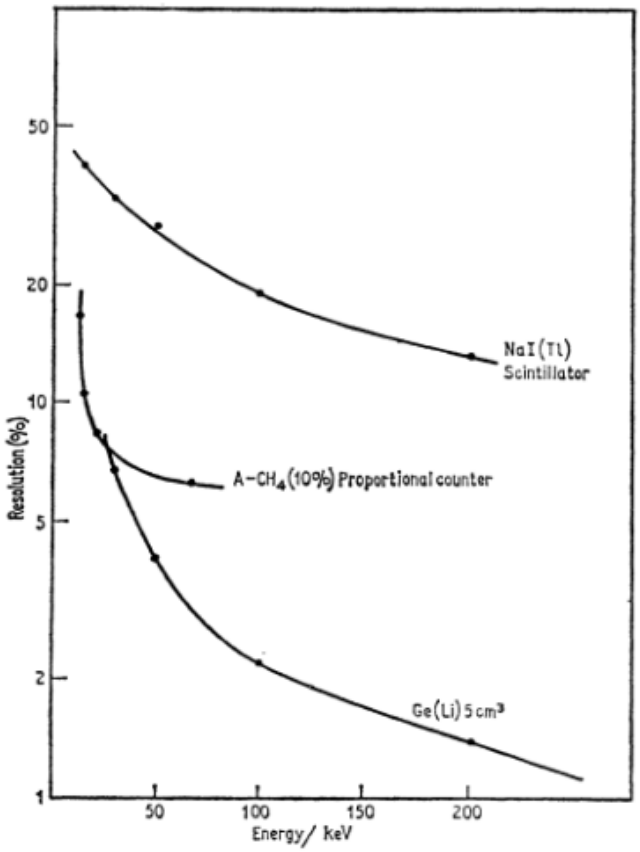


Figure 2-9: Comparison between most commonly used gamma rays [12]

For gamma rays below 40 keV, gas-filled proportional counters provide better resolution but with lower efficiency and generally reduced reliability. In certain cases, the radiation background can be minimized by using a suitable filter. For instance, a copper foil can absorb 27.5- and 31.0-keV X-rays from $^{125}$Te while transmitting most of the 35.5-keV gamma rays, due to the higher mass attenuation coefficient for the former [12].

The lithium-drifted germanium detector provides a highly resolved energy spectrum, as shown in Figure 2-9, though at the cost of low sensitivity and practical challenges. These detectors are particularly useful when multiple gamma rays of similar energy are present, as often seen in the complex decay schemes of heavier isotopes. However, their resolution significantly decreases with

lower energies, limiting their use to the higher end of the Mössbauer energy spectrum. Additional drawbacks include their high cost and the need for continuous cooling with liquid nitrogen [12].

**Cadmium Zinc Telluride (CZT) detector**

A semiconductor radiation detector, widely used in gamma spectroscopy, stands out from traditional scintillation detectors by directly converting incident gamma radiation into electrical signals. Made from Cadmium, Zinc, and Tellurium, CZT detectors are room-temperature semiconductor materials known for their excellent energy resolution for gamma rays. Their compact and portable nature makes them ideal for a variety of applications, including field measurements and portable radiation detection devices. The superior energy resolution of CZT detectors allows for the precise differentiation between gamma rays of varying energies, facilitating the identification of specific isotopes. Unlike some semiconductor detectors that require cryogenic cooling, CZT detectors operate effectively at room temperature, which simplifies their design and enhances their usability in a wide range of settings [38]. In Figure 2-10 there is an example of a CZT detector.

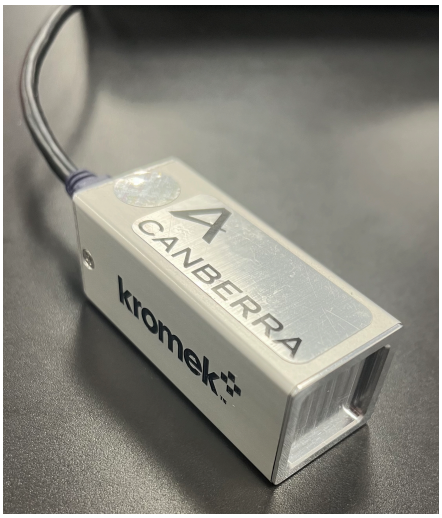


Figure 2-10: CZT Detector

There are several advantages to employing CZT detectors. These include having excellent charge collection properties, resulting in very good energy resolution. These detectors are often less sensitive to temperature changes compared to CdTe detectors and perform better at low energies.

**Cadmium Telluride (CdTe) detector**

Cadmium Telluride detectors are composed of Cadmium and Tellurium arranged in a cubic zinc blende structure, making it suitable for high-energy photon detection applications. Like CZT detectors, the CdTe detector operates based on the principle of direct photon-to-electron conversion, so high-energy photons interact with the CdTe material, creating electron-hole pairs. Under the influence of an electrical field, these charges drift toward respective electrodes, creating an electrical signal that is proportional to the energy of the incident photon. This collected signal is then amplified and processed to determine the energy and intensity of the detected radiation [39,40].

According to [39, 41] the energy resolution of this detector type can achieve values as low as 4% at 140 keV and around 5.9 keV for 662 keV, depending on the device configuration and operating conditions. Compared to scintillator detectors like NaI(Tl), CdTe has better energy resolution, often attributed to the high atomic number and density of the elements that make up the detector, which enhances photon absorption and minimizes scattering [38]. Their wide band gap (1.44 eV) allows operation at room temperature, avoiding the need for cryogenic cooling required using HPGe detectors. Additionally, the direct photon-to-electron conversion mechanism eliminates the need for bulky photomultiplier tubes, making CZT (shown in the Figure 2-11) and CdTe detectors compact, lightweight, and ideal for portable applications [40, 41].


Figure 2-11: CdTe detector and its Digital Pulse Processor [42]

**High-Purity Germanium (HPGe) detector**

This detector category works when gamma rays enter the detector, they interact with the germanium crystal via photoelectric absorption, Compton scattering or pair production, these interactions generate electron-hole pairs, just like the other semiconductors detectors. The detector is biased with a high voltage, creating an electric field that separates the electron-hole pairs. Electrons drift towards the anode, and holes toward the cathode. Finally, the resulting current pulse is proportional to the energy of the incident photon, then amplified and digitized for further

analysis. Furthermore, to maintain the high purity of the germanium crystal and prevent thermal noise from overwhelming the signal, the detector must be cooled to cryogenic temperatures, typically liquid nitrogen around 77 K [43, 44].

The energy resolution of HPGe detectors is exceptionally high, often cited as their most significant advantage. According to [43], Full Width Half Maximum (FWHM) values of approximately 0.2% at 1.33 MeV and [44] around 0.6 keV at 122 keV, allowing to distinguish between closely spaced energy peaks and providing accurate nuclide identification. The energy resolution is superior to scintillation detectors and even compound semiconductors like CdTe, making the HPGe detectors the gold standard for precision gamma ray spectroscopy. However, their crystal requires cooling to maintain the low leakage and high performance. Also their power and size requirements (see Figure 2-12) often make these detectors less convenient for portable applications. Finally, this type of detector can be expensive and require specialized handling and maintenance [44].

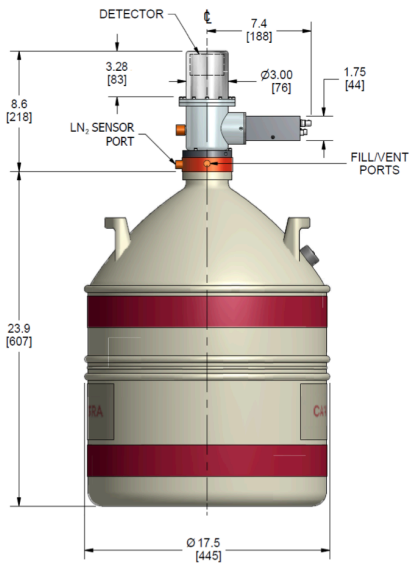


Figure 2-12: One example of HPGe detector and its dimension in inch[mm][45]

While each class of detector has strengths and weaknesses, CdTe detectors are particularly well-suited for the needs in Mössbauer spectroscopy of actinides. The HPGe detectors offer unmatched energy resolution for precise nuclide identification but are hindered by their requirement for cryogenic cooling, which limits their portability and versatility. The CZT detectors provide excellent charge collection and stable performance across temperatures, but their higher production cost and slightly lower gamma ray absorption efficiency at high energies make them less optimal than CdTe for the particular application considered here. The CdTe combines high gamma ray absorption efficiency due to their higher atomic number with better charge transport than CZT, and they are more cost-effective to manufacture, although they may require temperature stabilization for consistent performance. Overall, CdTe detectors provide the best balance of efficiency, energy resolution and practicality for this Mössbauer application.

# Chapter 3

# Methods

## Simulating the Mössbauer effect

Computer coding was developed to simulate the Mossbauer effect for various U isotopes. A copy of the code developed is provided in Appendix B. To simulate the Mossbauer effect it is necessary to simulate the gaussian distribution for the source using the $^{238}$Pu and $^{242}$Pu isotopes that will decay to $^{234}$U and $^{238}$U respectively, and emit a low energy gamma ray. So, using the same activity for both isotopes and their half-life parameters the Figure 3-1 below shows the behavior of the specific gamma ray emissions.

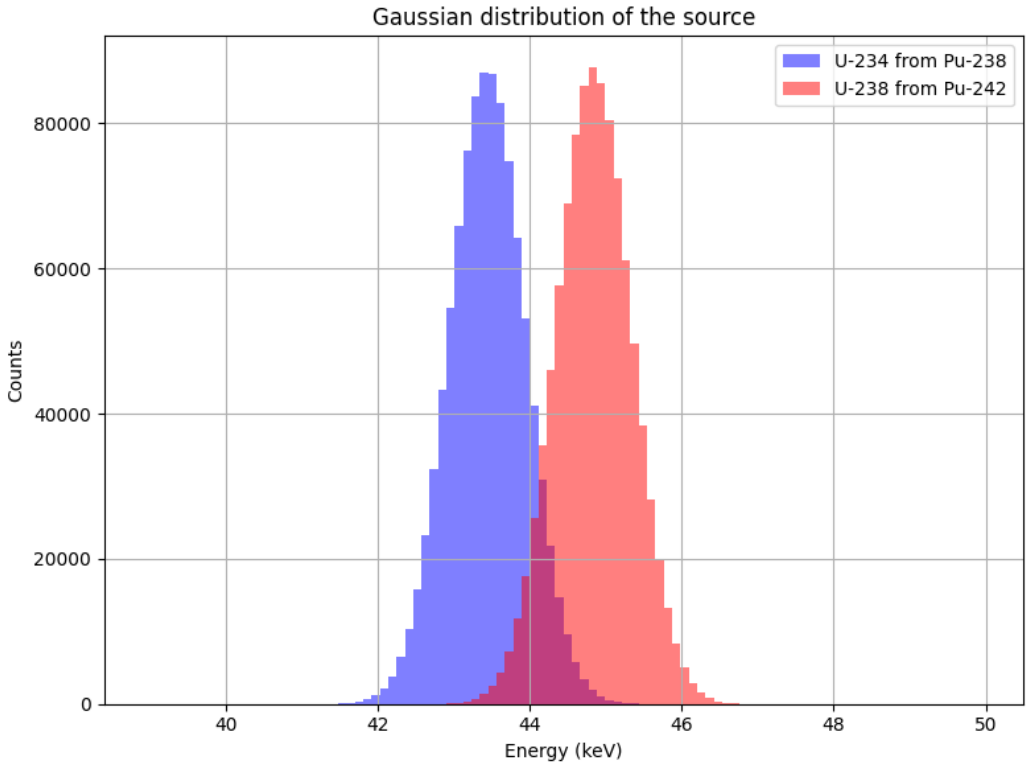


Figure 3-1: Gaussian distribution driven by the detector energy resolution for each gamma-ray peak from $^{242}$Pu and $^{238}$Pu

Once the gaussian distribution for the emission source is established it is important to know that the sample will also absorb the resonant energy gamma ray across a Gaussian distributed energy range. As the source moves back and forth on the linear stage of the Mossbauer spectrometer, the energy of the emitted gamma rays changes due to the Doppler effect from the moving stage, causing the emitted gamma rays to pass in and out of resonance relative to the stationary sample. The energy of the gamma rays from the source can be calculated using equation (3.1):

$$\delta E = \frac{velocity}{1000 \times c} \times E_{\gamma} \tag{3.1}$$

Where $\delta E$ is the energy shift due to the Doppler effect, $c$ is the speed of light, in this case multiplied by 1000 to convert the velocity from m/s to mm/s and $E_\gamma$ is the gamma energy. Then, using the number of counts for both isotopes and applying the desired velocity of 20 mm/s, the total counts measured by the detector without the presence of samples is shown in Figure 3-2.

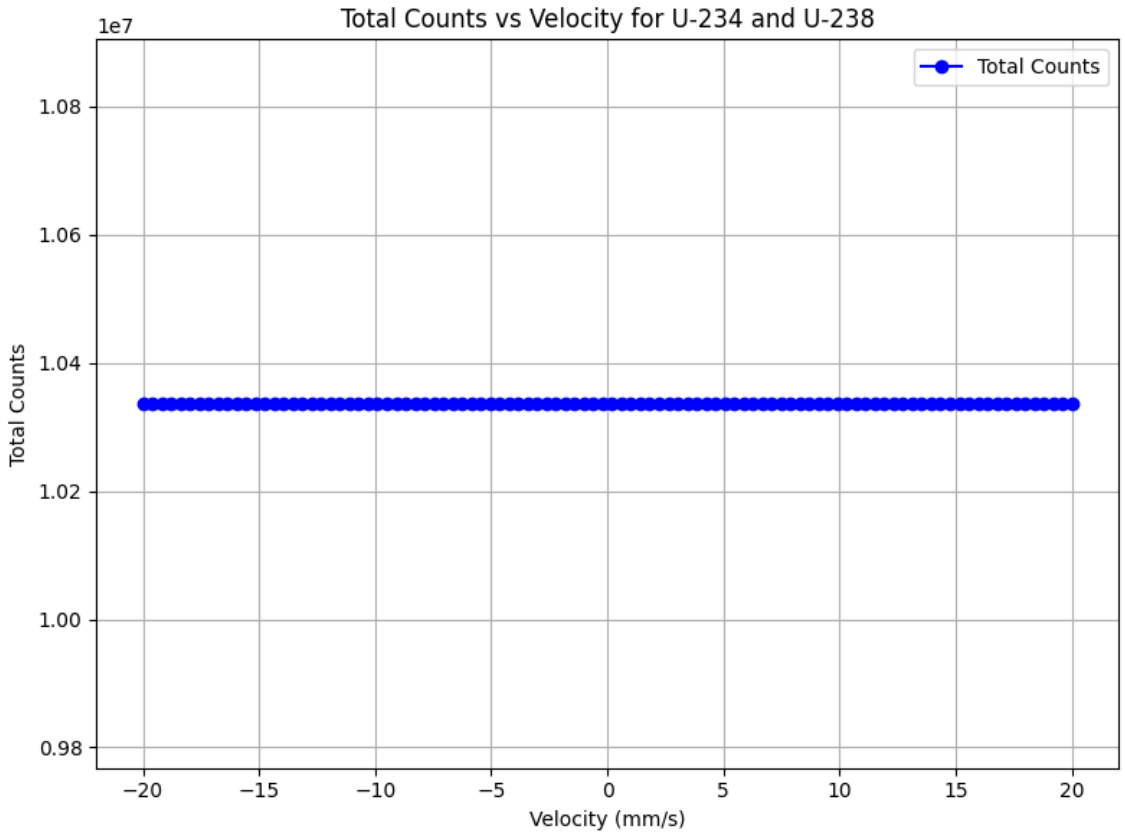


Figure 3-2: Total counts from a MS source (both isotopes) in function of the velocity transducer speed

Once the source was accurately modeled, the effect of the presence of a sample absorber containing the same ground state of the excited isotope within the source was simulated. The manner in which the absorbing isotope was modeled was similar to that of the source, without

including a doppler shift in the energy resonance for the sample since the sample is stationary relative to the source.

Detection of the Mössbauer effect is a function of the emission of the resonant gamma from the excited state nuclide making up the source and the absorption and re-emission of the resonant gamma by the ground state nuclide in the sample. Since the absorption of resonant gamma rays by the sample only occurs with resonant gamma rays that are incident to the detector, but re-emission of resonant gamma rays following absorption is omni-directional, the detector response during the Mössbauer effect is seen as a drop in the counts measured by the detector across the resonance region of that isotope. Figure 3-3 shows simulated detector response of an ideal case for the emission of resonant gammas by the excited $^{234}$U and $^{238}$U isotopes produced by the decays of $^{238}$Pu and $^{242}$Pu, each moving with an speed of 20 mm/s, followed by the absorption and re-emission of their resonant gammas by a sample containing ground states of $^{234}$U and $^{238}$U, both present in the same chemical form as the source materials. This signal is nearly indistinguishable from what would be expected from a conventional Mössbauer system based upon a single radioactive source of either $^{238}$Pu and $^{242}$Pu since the width, energy and timing of the energy resonances are nearly identical. Figure 3-3 is replicated in Figure 3-4, with the addition of a third dimension to resolve resonance effects as a function of energy.

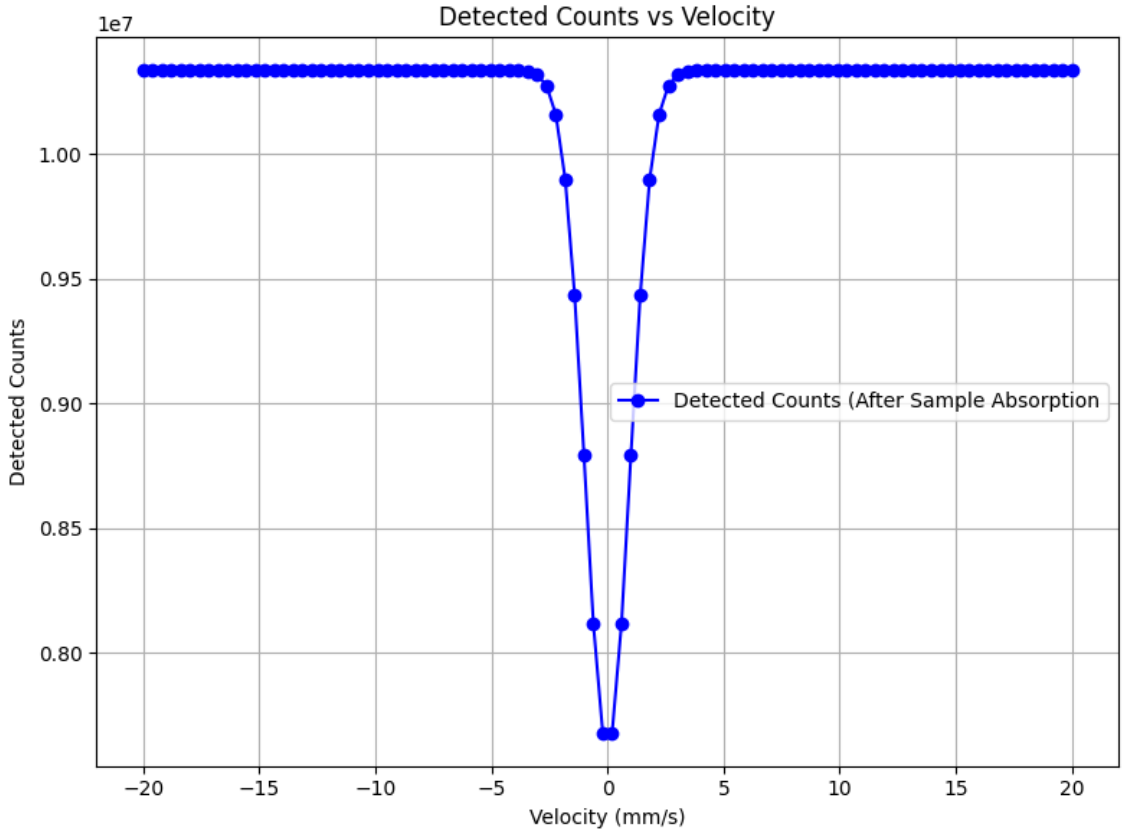


Figure 3-3: Drop in the number of counts representing the Mössbauer effect

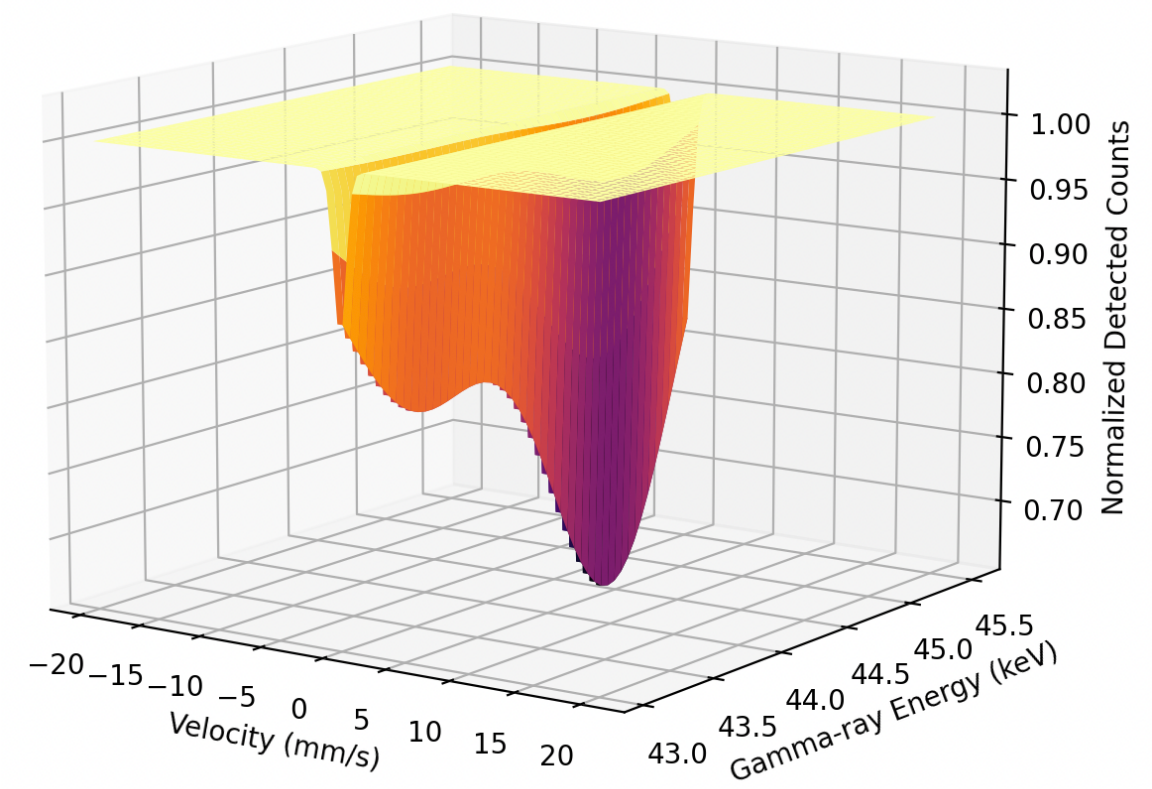


Figure 3-4: Mössbauer effect in a function of the gamma-ray energy

**Evaluating the Role of Detector Resolution for Estimating U Enrichment by UxMAS**

Model simulations were undertaken to evaluate the effect of detector resolution on the overall ability of the UxMAS system to estimate U enrichment. While Figure 3-4 more accurately represents the reality of the UxMAS Mossbauer spectrum, practically speaking, resolving the distribution of the absorbance valleys at a relative speed of 0 mm/s is essentially identical to resolving the individual resonance peaks by gamma spectroscopy. So for ease of the discussion, gamma spectra of the two resonance peaks for $^{234}U$ and $^{238}U$ are used to represent the challenge of resolving those signals by the UxMAS system. Figure 3-5 plots the simulated gaussian distribution

for a sample containing equal activities of $^{234}U$ and $^{238}U$, assuming a midpoint energy cutoff of 44.2 keV between the resonance peaks (resonance peaks of 43.5 keV and 44.7 keV for $^{234}U$ and $^{238}U$, respectively) [30].

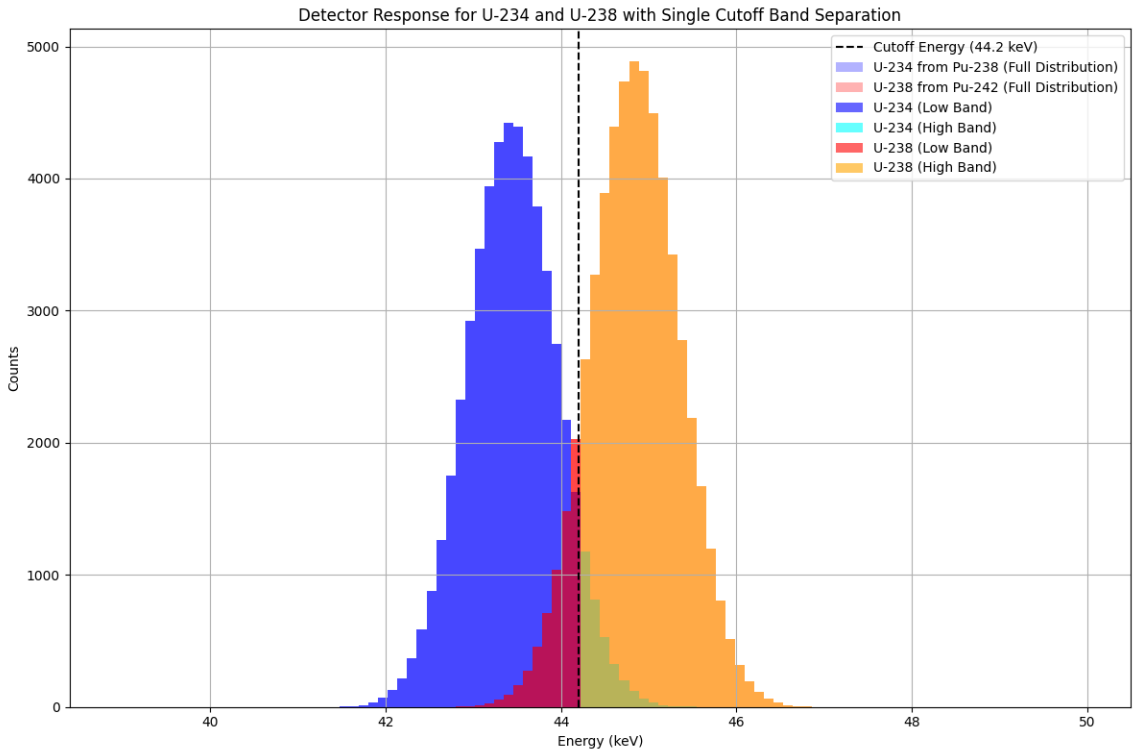


Figure 3-5: Separating the Low band and High band using the cutoff line determined in the middle

Selecting an appropriate energy of the cutoff between the resonance peaks of the two isotopes is critical since this will influence the calculation for the $^{234}U/^{238}U$ ratio, which is ultimately used to estimate the $^{235}U$ enrichment level of the sample. For the case above where the activity of $^{234}U$ and $^{238}U$ is the same and detection is achieved assuming 1% energy resolution, the total counts coming from the two isotopes assigned to represent $^{234}U$ and $^{238}U$ counts, respectively, is provided in Table 3-1.

Table 3-1: Data provided by the simulation in one of the runs

| | |
|---|---|
| **Total counts for U-234:** | 51194 |
| **Total counts for U-238:** | 56806 |
| **Counts in the low band for U-234 (<44.2 keV):** | 48901 |
| **Counts in the low band for U-238 (<44.2 keV):** | 6360 |
| **Counts in the high band for U-234 (>=44.2 keV):** | 3293 |
| **Counts in the high band for U-238 (>=44.2 keV):** | 50446 |
| **Overlapping counts in the low band:** | 5964 |
| **Overlapping counts in the high band:** | 3293 |

In Table 3-1, the total counts for $^{234}U$ in the low band is relatively similar to the total counts for $^{238}U$ in the high band, proving that the same activity for both will generate almost the same number of counts for each gamma-ray energy. However, this is not the case as the relative activities of the $^{234}U$ and $^{238}U$ start to differ significantly from one another. In that case, the isotope with the lower activity will be overestimated due to the disproportionate number of counts incorrectly binned from the other isotope.

Typical isotope distributions for uranium with different levels of $^{235}U$ enrichment are provided from the U.S. DOE in Table 3-2. These values show a strong trend in the isotopic distributions of $^{234}U$, $^{235}U$ and $^{238}U$ (Figure 3-6). Using this data, it is possible to extrapolate the atom percent distributions for $^{234}U$ and $^{238}U$ (Table 3-3).

Table 3-2: Data from DOE $^{235}U$ enrichment and others Uranium isotopes percentage [1,2]

| Enrichment | $^{235}U$ | $^{234}U$ | $^{236}U$ | $^{238}U$ |
|---|---|---|---|---|
| 93% | **93%** | **1.0%** | **0.445%** | **5.555%** |
| 50% | **50%** | **0.425%** | **0.231%** | **49.344%** |
| 4% | **4%** | **0.0334%** | **0.0154%** | **95.9512%** |
| 0.9% | **0.9%** | **0.00948%** | **0.00325%** | **99.08727%** |
| Natural Uranium | **0.711%** | **0.00541%** | **0%** | **99.28359%** |
| Depleted Uranium | **0.2%** | **0.00356%** | **0%** | **99.79644%** |

Table 3-3: Extrapolated atom percentage for each Uranium isotope using the data provided

| **Enrichment [%]** | $^{235}U$ | $^{234}U$ | $^{236}U$ | $^{238}U$ |
|---|---|---|---|---|
| **45%** | 45 | 0.38 | 0.27 | 54.36 |
| **40%** | 40 | 0.32 | 0.22 | 59.46 |
| **35%** | 35 | 0.27 | 0.18 | 64.55 |
| **30%** | 30 | 0.23 | 0.14 | 69.63 |
| **25%** | 25 | 0.19 | 0.11 | 74.70 |
| **20%** | 20 | 0.16 | 0.09 | 79.75 |

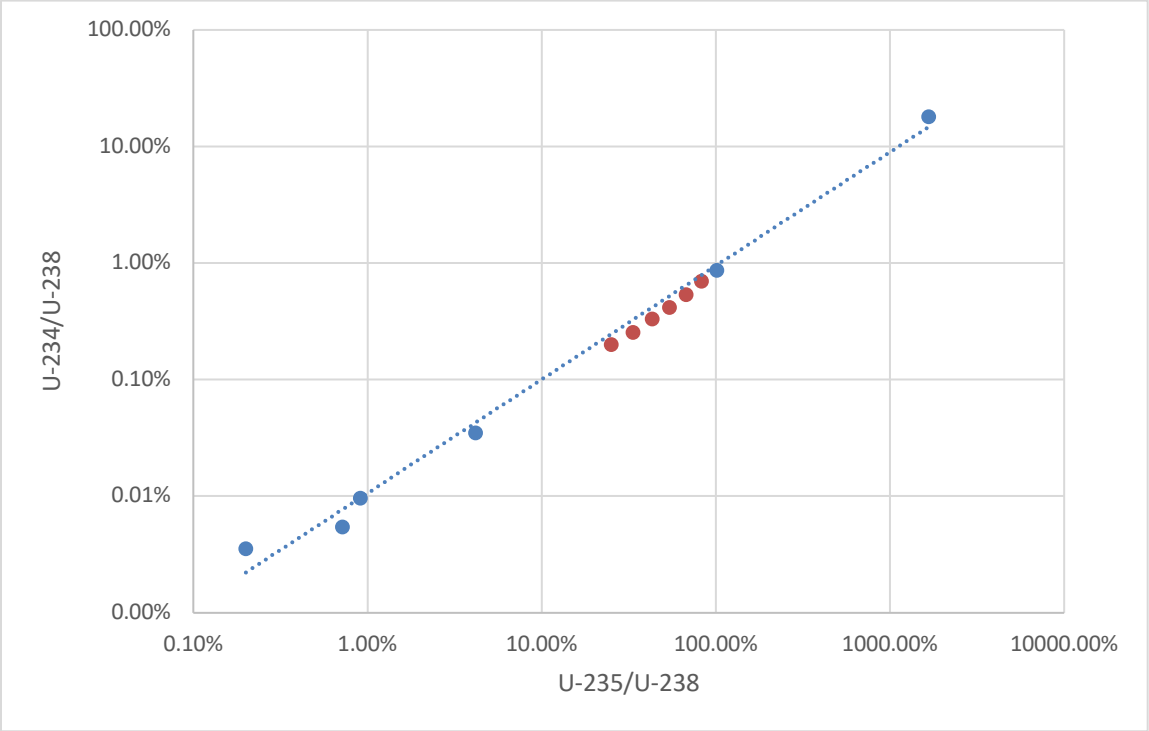


Figure 3-6: Enrichment ratio of $^{234}U/^{238}U$ vs enrichment ratio of $^{235}U/^{238}U$

The data provided in Tables 3-2 and 3-3 were then used to create models of the gamma spectra around the resonance peaks for $^{234}U$ and $^{238}U$ in order to determine what level of detector resolution was required by the UxMAS system to make a inferences about U enrichment based upon $^{234}U$ and $^{238}U$ Mossbauer response.

Two different approaches were used to define a low and high gamma ray energy band to represent the relative $^{234}U$ and $^{238}U$ activities, respectively. These low and high energy bands were then used to estimate the $^{234}U/^{238}U$ activity ratio, which in turn was used to provide a measure of the $^{235}U$ enrichment based upon the relationship previously shown in Figure 3-6. One approach was to define the low (section C shown in solid bold blue) and high energy (section B shown in solid bold orange) bands by the midpoint energy between the peak energy resonances for $^{234}U$ and $^{238}U$ as shown in Figure 3-7. Using this method, the portion of the counts incorrectly binned in the low

energy bin from $^{238}U$ resonance include section A shown in red shading, while the portion of the counts coming from $^{234}U$ resonance incorrectly binned in the high energy band are labeled section D and shown in olive shading. The second approach defines the low energy band to include gamma counts below the peak energy resonance of $^{234}U$ (shown in solid bold blue) and the high energy band to include counts above the peak energy resonance for $^{238}U$ (shown in solid bold orange shading), which is shown in Figure 3-8. The uncertainty in these approaches was defined according to Equation 3-2.

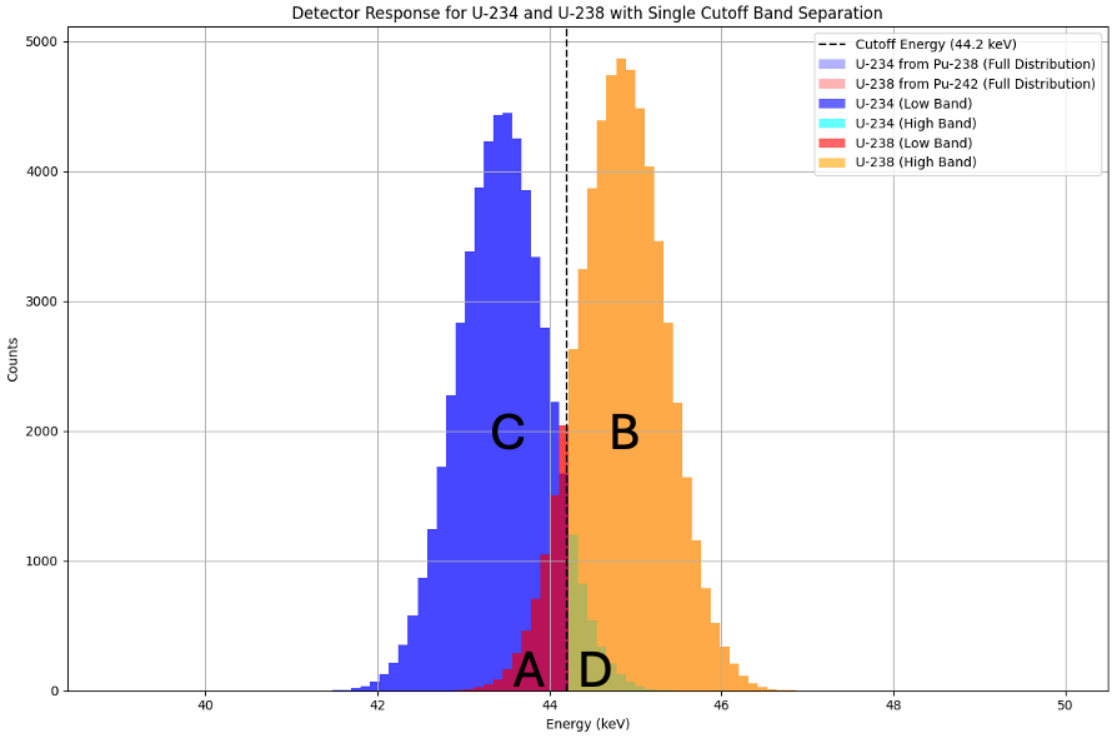


Figure 3-7: Parameters to calculate the uncertainty for the case using one cutoff line

Relative uncertainties for the two approaches to define low and high energy bands to represent $^{234}U$ and $^{238}U$ activities is defined below:

$$\sigma = R \times \sqrt{\left(\frac{A}{C}\right)^2 + \left(\frac{D}{B}\right)^2} \tag{3.2}$$

Where $R$ is the $^{234}U/^{238}U$ ratio, $A$ is the counts for $^{238}U$ in the low band, $B$ is the counts for $^{238}U$ in the high band, and $C$ is the counts for $^{234}U$ in the low band, $D$ is the counts for $^{234}U$ in the high band.

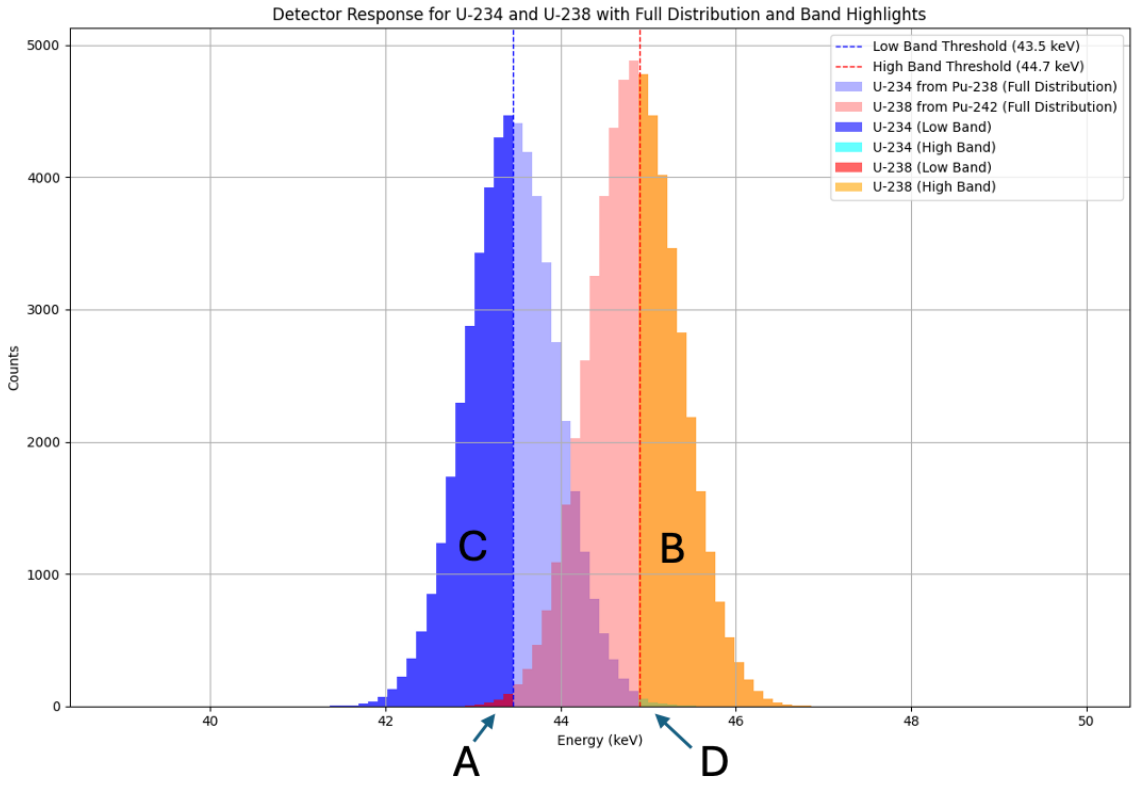


Figure 3-8: Parameters to calculate the uncertainty for the case using two cutoff lines in each isotope peak

# Chapter 4

# Results

Model simulations were undertaken to investigate the ability to estimate enrichment of U samples by simultaneously measuring $^{234}U$ and $^{238}U$ by MS. Important nuclear data describing Mossbauer transitions for these isotopes are provided Table in the Appendix. From this Table, several challenges arise when attempting to measure $^{234}U$ and $^{238}U$ simultaneously by MS. First, practically speaking, Pu parents are used to access the excited states of both U isotopes, making the handling of sources for U MS challenging. Secondly, the energies of the resonances for $^{234}U$ and $^{238}U$ are quite similar at 43.49 and 44.91, respectively [48]. Third, the natural abundance of $^{234}U$ is more than 4 orders of magnitude lower than that of $^{238}U$. Fourth, the half-lives of the excited states of both U isotopes are relatively short at 0.025 ns for $^{234}U$ and 0.021 ns for $^{238}U$ [48]. The short half-life's of the excited states of $^{234}U$ and $^{238}U$ is inversely related to their natural line widths, leading to rather large natural line widths of their resonances of 24 mm $s^{-1}$ and 27 mm $s^{-1}$, respectively. Fifth, the resonant absorption cross-section for $^{234}U$ and $^{238}U$ is also very low at 4 mbarns [32] and 10 mbarns [12], respectively. All of these factors make the simultaneous measurement of $^{234}U$ and $^{238}U$ by MS extremely challenging. Simulations were undertaken to estimate detector response of resonance emission by $^{234}U$ and $^{238}U$ excited states as a function of detector resolution and to optimize a method for deconvoluting peaks from both isotopes.

As previously discussed in chapter 3, there is a predictable relationship between the relative abundances of $^{234}U$ and $^{235}U$ within enriched and depleted U (see Figure 4-1). This manifests into a predictable relationship between $^{234}U$ and $^{238}U$ as a function of $^{235}U$ enrichment (Figure 4-1) at enrichment levels up to 60%. This indicates that the abundance of $^{238}U$ is expected to be at least

two orders of magnitude greater than $^{234}U$ within enriched material, creating a challenge when attempting to deconvolute resonance peaks that are less than 2 keV separated in energy. One potential solution to this issue is to use a $^{242}Pu/^{238}Pu$ mixed radioactive source that is lower in $^{242}Pu$ activity relative to that of $^{238}Pu$.It is indicated in [48], a 2 mCi $^{242}Pu$ source provides sufficient activity to generate quality $^{238}U$ Mossbauer spectra over reasonable count times of less than one week. Based on this, the lower bounds for the minimum activity of a source for U MS is taken as 1 mCi, with a upper bounds taken as 100 mCi based upon pragmatic considerations for source handling.

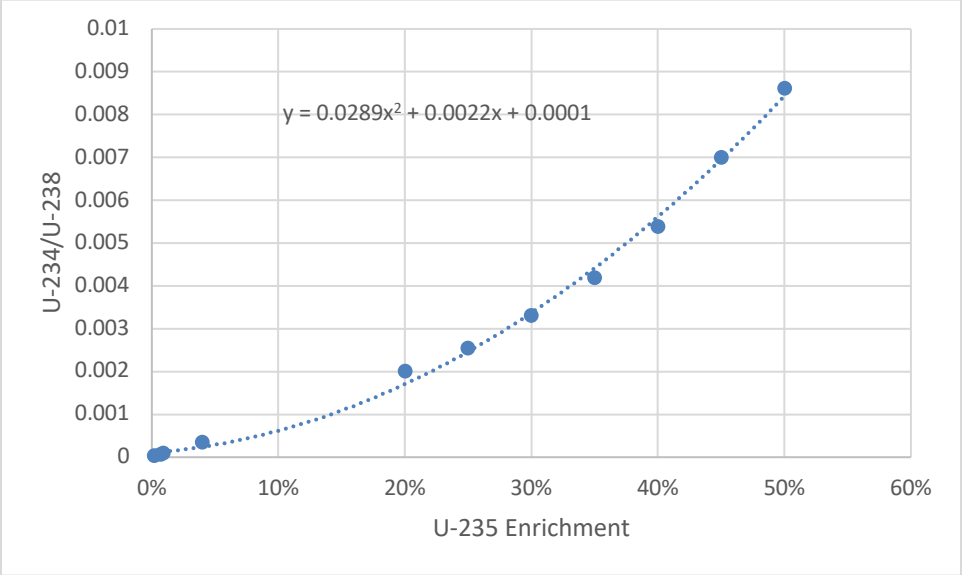


Figure 4-1: Atom ratio of $^{234}U/^{238}U$ as a function of $^{235}U$ enrichment. Dashed line represents polynomial fit to the data.

Resonance peaks of $^{234}U$ and $^{238}U$ were modeled as a function of gamma detector resolution to investigate the ability of gamma ray spectroscopy for separating these peaks based upon their energies. Figure 10 shows the simulated gamma spectra for the resonance peaks of $^{234}U$ and $^{238}U$ using the midpoint energy as the cutoff between the two peaks at 44.2 keV, assuming a detector

resolution of 1 keV FWHM. The figure was generated using a sample assumed to contain 93% enriched of $^{235}$U, and two radioactive Mossbauer sources of $^{238}$Pu and $^{242}$Pu, for which the $^{242}$Pu activity was assumed to be 20% of that of the $^{238}$Pu source.

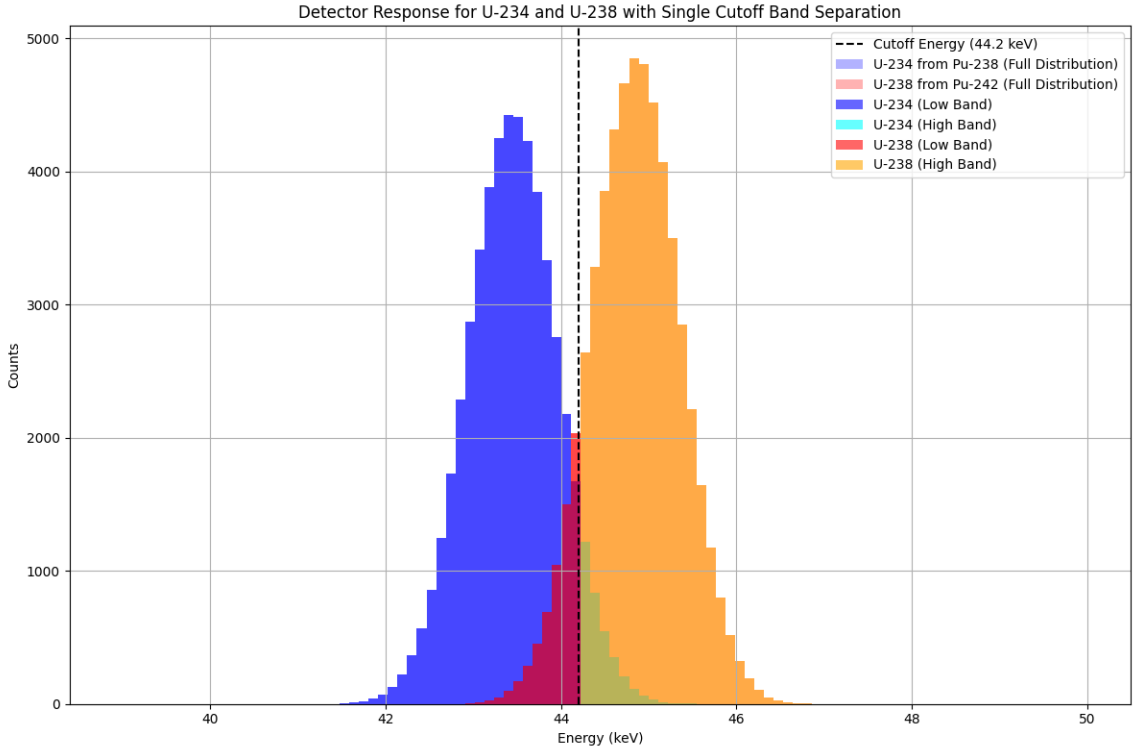


Figure 4-2: Energy distribution for 93% of $^{235}$U using 20% $^{242}$Pu in the source with one cutoff line at 44.2 keV

The portion of the peak shown in blue in Figure 4-2 were attributed to $^{234}$U counts, whereas the portion in orange were attributed to $^{238}$U counts. Counts coming from $^{234}$U resonance misassigned to $^{238}$U and counts coming from $^{238}$U resonance misassigned to $^{234}$U by using a midpoint energy cutoff to define low and high bands are shown in green and red, respectively. Figures 4-3, 4-4, and 4-5 simulate results for samples with a $^{235}$U isotopic abundance of 50%, 45%, and 0.2%, respectively.

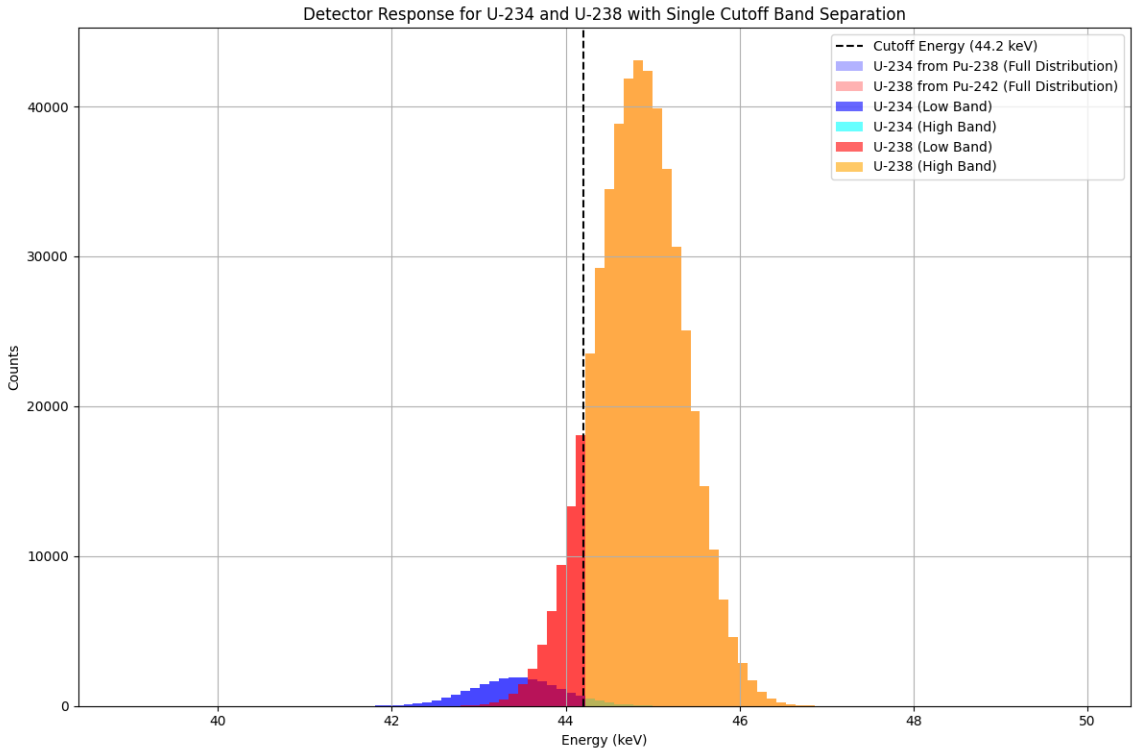


Figure 4-3: Energy distribution for 50% of $^{235}U$ using 20% $^{242}Pu$ in the source with one cutoff line at 44.2 keV

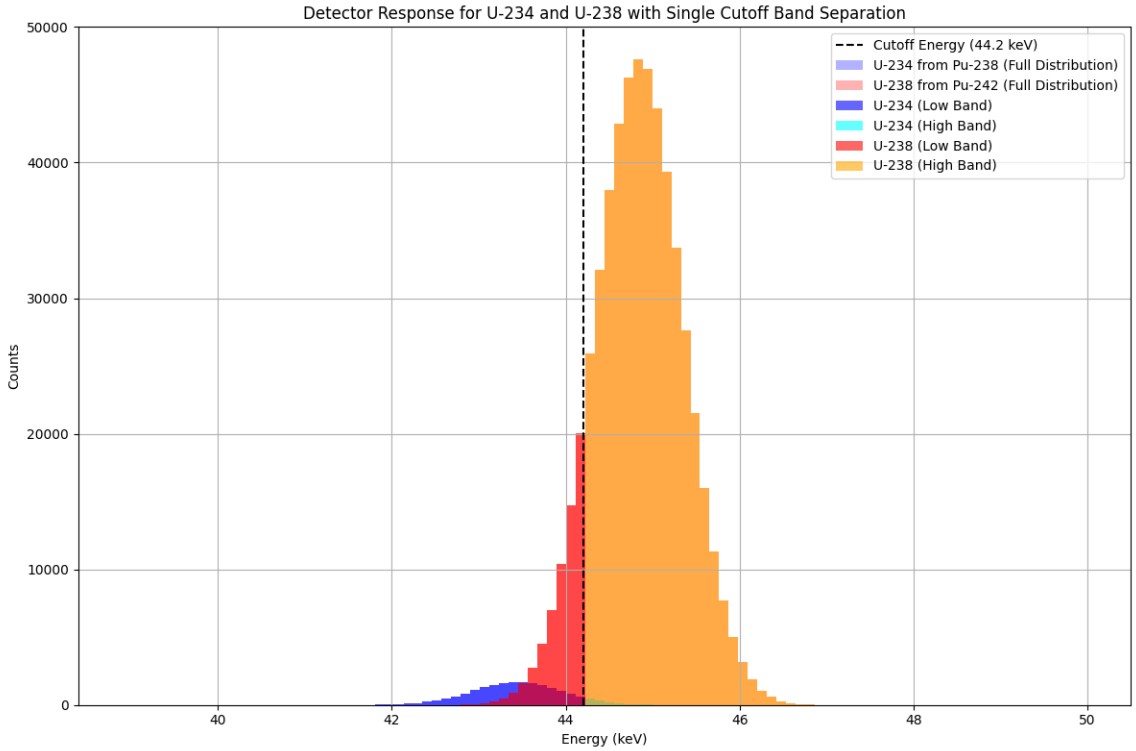


Figure 4-4: Energy distribution for 45% of $^{235}U$ using 20% $^{242}Pu$ in the source with one cutoff line at 44.2 keV

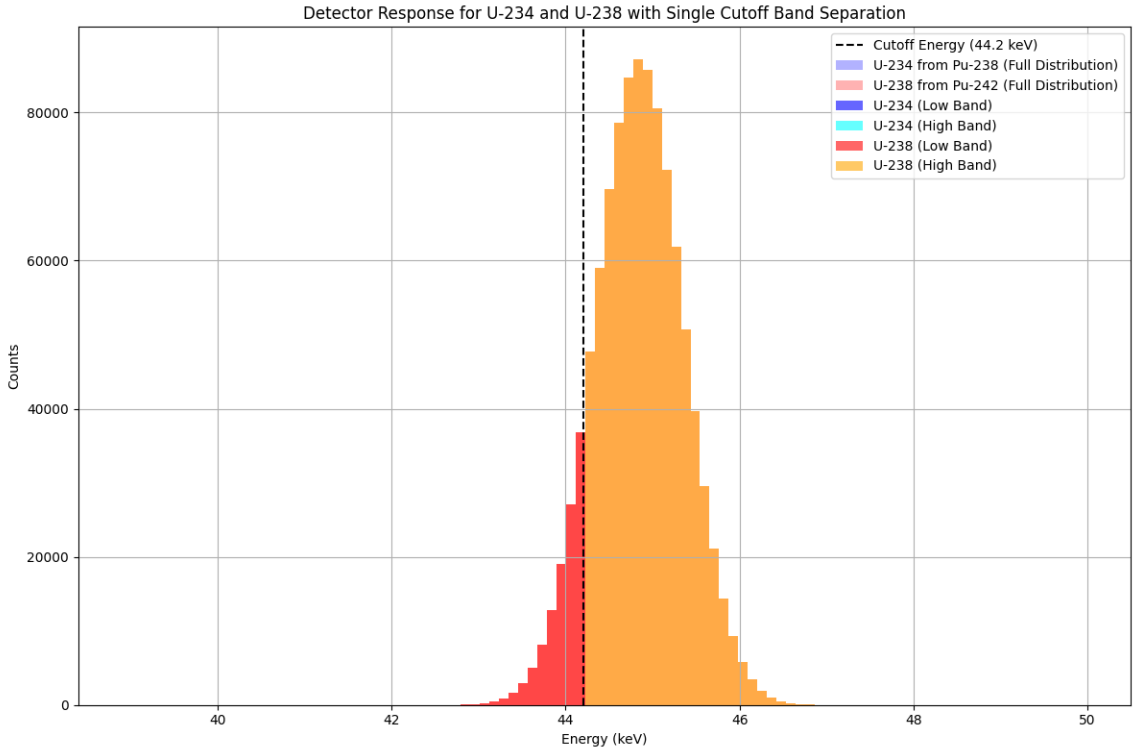


Figure 4-5: Energy distribution for 0.2% of $^{235}$U using 20% $^{242}$Pu in the source with one cutoff line at 44.2 keV

Clearly, counts assigned to the $^{234}$U low band portion of the spectra become difficult to quantify below a $^{235}$U enrichment level of roughly 45% using the mid energy cutoff of 44.2 keV. Tables 4-1 to 4-5 summarize similar results as shown in Figures 4-2 to 4-5 for sample $^{235}$U enrichments ranging from depleted to 93%, assuming the activity of the $^{242}$Pu source ranges in values from 100-1% of that of the $^{238}$Pu activity. Uncertainty related to the low to high band ratio ($\sigma$) was calculated based upon the following equation (3.2) previously discussed.

Table 4-1: Data considering the cutoff line at 44.2 keV for 100% of $^{242}$Pu activity

| Enrichment [%] | Total Counts U234 - Low band | Total Counts U234 - high band | Total Counts U238 - low band | Total Counts U238 - high band | Ratio Low band/High band | Absolut Uncertainty | Relative Uncertainty |
|---|---|---|---|---|---|---|---|
| **93%** | 48803 | 3392 | 32155 | 251952 | 0.18371599 | 0.65901096 | 61.2880193 |
| **50%** | 20734 | 1440 | 285382 | 2238479 | 0.00878575 | 13.7639626 | 688.198129 |
| **45%** | 18568 | 1253 | 313913 | 2466509 | 0.00712877 | 16.9061288 | 760.775797 |
| **40%** | 15627 | 1061 | 343145 | 2698141 | 0.00548715 | 21.9584693 | 878.338773 |
| **35%** | 13200 | 877 | 373330 | 2928300 | 0.00426365 | 28.2825758 | 989.890152 |
| **30%** | 11241 | 744 | 402958 | 3158508 | 0.00336519 | 35.8471666 | 1075.415 |
| **25%** | 9266 | 634 | 432066 | 3388723 | 0.00259109 | 46.629182 | 1165.72955 |
| **20%** | 7803 | 531 | 460726 | 3618364 | 0.0020431 | 59.0447264 | 1180.89453 |
| **4%** | 1627 | 99 | 553959 | 4353805 | 0.00035169 | 340.478795 | 1361.91518 |
| **0.90%** | 451 | 28 | 572926 | 4495245 | 9.4511E-05 | 1270.3459 | 1143.31131 |
| **0.70%** | 256 | 12 | 574246 | 4503964 | 5.2775E-05 | 2243.14844 | 1594.87854 |
| **0.20%** | 168 | 6 | 576491 | 4527951 | 3.4088E-05 | 3431.49405 | 686.29881 |

Table 4-2: Data considering the cutoff line at 44.2 keV for 80% of $^{242}$Pu activity

| Enrichment [%] | Total Counts U234 - Low band | Total Counts U234 - high band | Total Counts U238 - low band | Total Counts U238 - high band | Ratio Low band/High band | Absolut Uncertainty | Relative Uncertainty |
|---|---|---|---|---|---|---|---|
| **93%** | 48912 | 3283 | 25427 | 201858 | 0.2296456 | 0.52010633 | 48.3698887 |
| **50%** | 20731 | 1435 | 228026 | 1791060 | 0.01097823 | 10.9992765 | 549.963824 |
| **45%** | 18562 | 1256 | 251386 | 1972949 | 0.00890963 | 13.5430449 | 609.437023 |
| **40%** | 15637 | 1054 | 274682 | 2158341 | 0.00686019 | 17.5661572 | 702.646288 |
| **35%** | 13167 | 908 | 298694 | 2342606 | 0.00532882 | 22.685046 | 793.976608 |
| **30%** | 11250 | 737 | 321639 | 2527528 | 0.00420719 | 28.5901333 | 857.704 |
| **25%** | 9301 | 602 | 345166 | 2711463 | 0.00323984 | 37.1106333 | 927.765832 |
| **20%** | 7825 | 513 | 368686 | 2894582 | 0.00255511 | 47.1164217 | 942.328435 |
| **4%** | 1603 | 125 | 443705 | 3482501 | 0.00044012 | 276.796631 | 1107.18653 |
| **0.90%** | 459 | 19 | 457826 | 3596706 | 0.00011789 | 997.442266 | 897.698039 |
| **0.70%** | 258 | 11 | 458812 | 3603750 | 6.6214E-05 | 1778.34109 | 1264.40051 |
| **0.20%** | 163 | 10 | 461599 | 3621951 | 4.2365E-05 | 2831.89571 | 566.379141 |

Table 4-3: Data considering the cutoff line at 44.2 keV for 60% of $^{242}$Pu activity

| Enrichment [%] | Total Counts U234 - Low band | Total Counts U234 - high band | Total Counts U238 - low band | Total Counts U238 - high band | Ratio Low band/High band | Absolut Uncertainty | Relative Uncertainty |
|---|---|---|---|---|---|---|---|
| **93%** | 48944 | 3250 | 19204 | 151251 | 0.30620398 | 0.39295471 | 36.5447883 |
| **50%** | 20792 | 1375 | 170896 | 1343410 | 0.01463839 | 8.21931518 | 410.965759 |
| **45%** | 18555 | 1266 | 187757 | 1480489 | 0.01188134 | 10.1189437 | 455.352467 |
| **40%** | 15640 | 1048 | 206193 | 1618569 | 0.0091453 | 13.1836957 | 527.347827 |
| **35%** | 13188 | 889 | 224127 | 1756839 | 0.00710613 | 16.994768 | 594.816879 |
| **30%** | 11196 | 791 | 241916 | 1894951 | 0.00560961 | 21.6073598 | 648.220793 |
| **25%** | 9263 | 637 | 258918 | 2033545 | 0.0043185 | 27.9518515 | 698.796286 |
| **20%** | 7749 | 585 | 277257 | 2170188 | 0.00340518 | 35.7797135 | 715.59427 |
| **4%** | 1606 | 120 | 332607 | 2612041 | 0.00058615 | 207.10274 | 828.410959 |
| **0.90%** | 449 | 27 | 342942 | 2697949 | 0.00015653 | 763.790646 | 687.411581 |
| **0.70%** | 253 | 14 | 344295 | 2702622 | 8.763E-05 | 1360.8498 | 967.564209 |
| **0.20%** | 166 | 5 | 345897 | 2716760 | 5.5834E-05 | 2083.71687 | 416.743373 |

Table 4-4: Data considering the cutoff line at 44.2 keV for 40% of $^{242}$Pu activity

| Enrichment [%] | Total Counts U234 - Low band | Total Counts U234 - high band | Total Counts U238 - low band | Total Counts U238 - high band | Ratio Low band/High band | Absolut Uncertainty | Relative Uncertainty |
|---|---|---|---|---|---|---|---|
| **93%** | 48846 | 3343 | 12900 | 100734 | 0.45927275 | 0.26617227 | 24.7540209 |
| **50%** | 20722 | 1447 | 114019 | 895515 | 0.02195964 | 5.50231662 | 275.115831 |
| **45%** | 18542 | 1277 | 126102 | 98055 | 0.08841571 | 6.80089695 | 306.040363 |
| **40%** | 15606 | 1084 | 137067 | 1079430 | 0.01371972 | 8.78296815 | 351.318726 |
| **35%** | 13236 | 841 | 149342 | 1171296 | 0.01065924 | 11.283016 | 394.905561 |
| **30%** | 11225 | 762 | 160370 | 1264201 | 0.00841446 | 14.2868597 | 428.605791 |
| **25%** | 9268 | 630 | 172983 | 1355317 | 0.00647648 | 18.6645447 | 466.613617 |
| **20%** | 7786 | 550 | 183538 | 1448085 | 0.00510902 | 23.572823 | 471.45646 |
| **4%** | 1629 | 99 | 221927 | 1741163 | 0.00088024 | 136.235114 | 544.940454 |
| **0.90%** | 449 | 30 | 229203 | 1798050 | 0.00023628 | 510.474388 | 459.426949 |
| **0.70%** | 258 | 10 | 229650 | 1801620 | 0.00013194 | 890.116279 | 632.872674 |
| **0.20%** | 161 | 7 | 230415 | 1811349 | 8.2282E-05 | 1431.14907 | 286.229814 |

Table 4-5: Data considering the cutoff line at 44.2 keV for 20% of $^{242}$Pu activity

| Enrichment [%] | Total Counts U234 - Low band | Total Counts U234 - high band | Total Counts U238 - low band | Total Counts U238 - high band | Ratio Low band/High band | Absolut | Relative |
|---|---|---|---|---|---|---|---|
| **93%** | 48784 | 3407 | 6305 | 50499 | 0.91879093 | 0.14579286 | 13.5587355 |
| **50%** | 20812 | 1359 | 56946 | 447809 | 0.04392428 | 2.73621156 | 136.810578 |
| **45%** | 18574 | 1248 | 62676 | 493386 | 0.0356471 | 3.37439526 | 151.847787 |
| **40%** | 15620 | 1068 | 68375 | 539865 | 0.02743654 | 4.37740122 | 175.096049 |
| **35%** | 13188 | 886 | 74612 | 585693 | 0.02131439 | 5.65756769 | 198.014869 |
| **30%** | 11231 | 758 | 80350 | 631923 | 0.01683203 | 7.15430515 | 214.629154 |
| **25%** | 9269 | 633 | 85771 | 678367 | 0.01295839 | 9.25353333 | 231.338333 |
| **20%** | 7783 | 553 | 91738 | 724064 | 0.01021817 | 11.7869716 | 235.739433 |
| **4%** | 1617 | 108 | 110914 | 870619 | 0.00175745 | 68.5924552 | 274.369821 |
| **0.90%** | 449 | 31 | 114295 | 899322 | 0.00047355 | 254.554566 | 229.099109 |
| **0.70%** | 248 | 20 | 114879 | 900743 | 0.00026388 | 463.221774 | 329.350681 |
| **0.20%** | 162 | 8 | 115337 | 905531 | 0.00016652 | 711.95679 | 142.391358 |

Table 4-6: Data considering the cutoff line at 44.2 keV for 10% of $^{242}$Pu activity

| Enrichment [%] | Total Counts U234 - Low band | Total Counts U234 - high band | Total Counts U238 - low band | Total Counts U238 - high band | Ratio Low band/High band | Absolut Uncertainty | Relative Uncertainty |
|---|---|---|---|---|---|---|---|
| **93%** | 48902 | 3289 | 3199 | 25194 | 1.83816434 | 0.14601997 | 13.5798574 |
| **50%** | 20753 | 1420 | 28226 | 224136 | 0.08786188 | 1.36010727 | 68.0053636 |
| **45%** | 18574 | 1247 | 31539 | 246488 | 0.07129164 | 1.69802627 | 76.4111823 |
| **40%** | 15607 | 1083 | 34094 | 270015 | 0.05488164 | 2.18453626 | 87.3814505 |
| **35%** | 13169 | 908 | 37618 | 292525 | 0.0426391 | 2.85655875 | 99.9795563 |
| **30%** | 11230 | 763 | 40071 | 316059 | 0.0336759 | 3.56821097 | 107.046329 |
| **25%** | 9260 | 640 | 43181 | 338878 | 0.02591223 | 4.66317533 | 116.579383 |
| **20%** | 7804 | 529 | 45801 | 362088 | 0.02042958 | 5.86891356 | 117.378271 |
| **4%** | 1624 | 102 | 55334 | 435424 | 0.00351701 | 34.0726601 | 136.29064 |
| **0.90%** | 443 | 36 | 57505 | 449291 | 0.00094515 | 129.808126 | 116.827314 |
| **0.70%** | 257 | 12 | 57364 | 450438 | 0.00052973 | 223.206226 | 158.699626 |
| **0.20%** | 162 | 7 | 57321 | 453104 | 0.0003311 | 353.833333 | 70.7666667 |

While lowering the activity of the $^{242}$Pu source, relative to that of the $^{238}$Pu source reduced uncertainties of the measured low band to high band ratio, the uncertainties associated with all R values were greater than 100%. This indicated that 1% energy resolution, using a midpoint energy cutoff between low and high energy bands to represent resonance energy counts from $^{234}$U and $^{238}$U, was ineffective for estimating $^{235}$U enrichment based upon the ratio of the low to high band counts.

A second approach to defining low and high energy bands to represent resonance energy counts from $^{234}$U and $^{238}$U was also studied. In this case, rather than choosing the midpoint energy to define low and high bands, the low band was defined as any counts of an energy at or below the peak energy of the $^{234}$U (43.5 keV) and the high band was defined as any counts at or above the peak resonance energy of $^{238}$U (44.7 keV). This approach reduced count rates but increased the signal to noise and decreased overall uncertainties associated with measuring R values. Figures 4-6 to 4-9 summarize results using the new band definitions for U samples of different $^{235}$U enrichments, assuming a $^{242}$Pu source activity of 20% of that of the $^{238}$Pu source. Tables 4-7 to 4-12 summarize simulation results using the new low and high band definitions assuming activities of the $^{242}$Pu source ranging from 100%-10% relative to the $^{238}$Pu source.

In addition, in Figures 4-10 to 4-15, it is possible to visualize the enrichment as a function of the ratio between the low band and high band counts at various levels of activity of $^{242}$Pu source relative to that of the $^{238}$Pu source. As the $^{242}$Pu source activity decreases relative to $^{238}$Pu activity, the ability to measure $^{234}$U in the presence of excess $^{238}$U is enhanced.

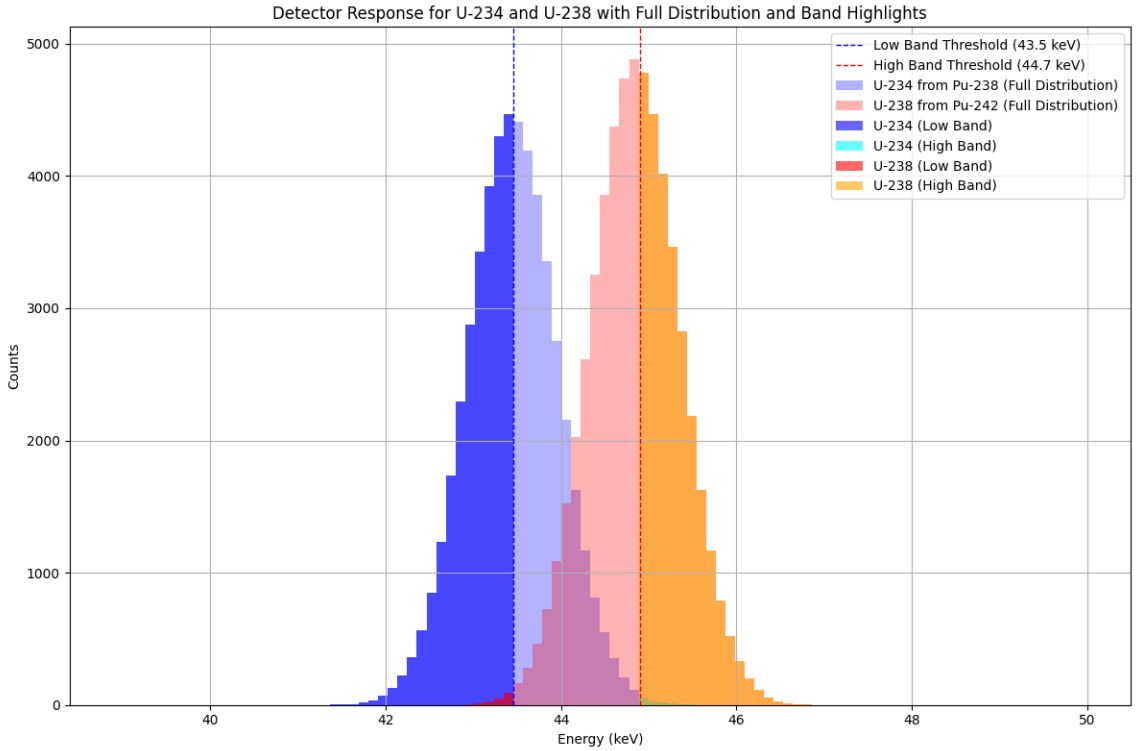


Figure 4-6: Energy distribution for 93% of $^{235}U$ using 20% $^{242}Pu$ in the source with two cutoff lines at 43.5 keV and 44.7 keV

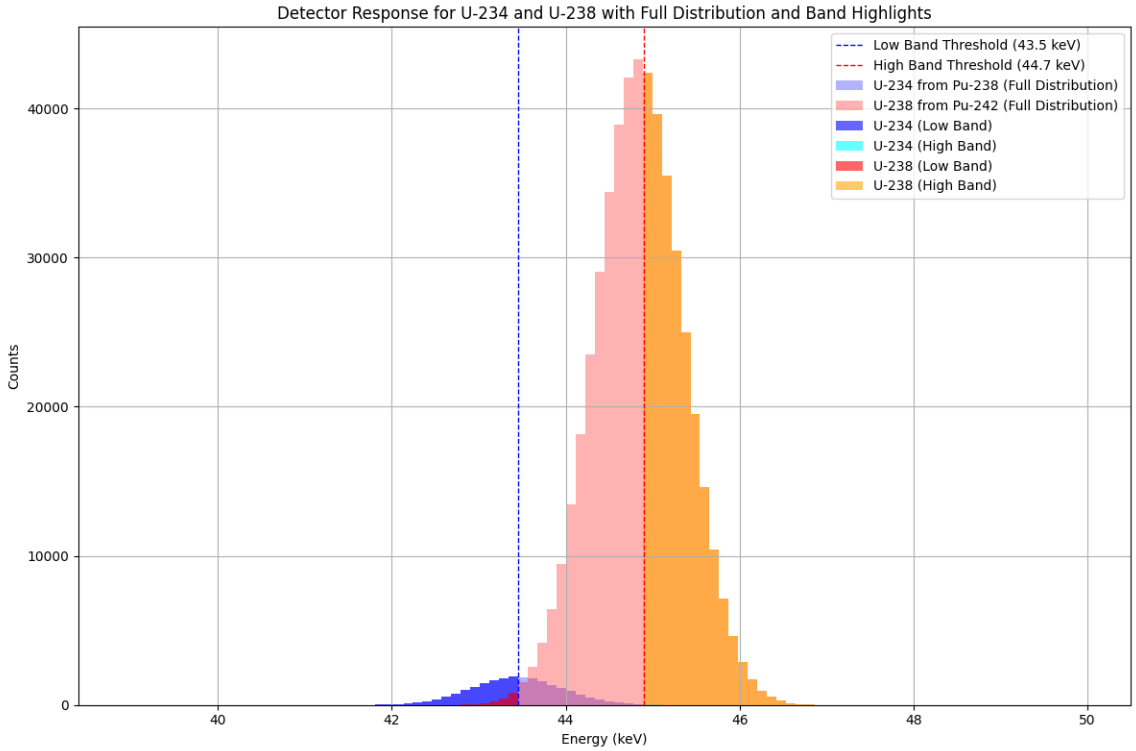


Figure 4-7: Energy distribution for 50% of $^{235}U$ using 20% $^{242}Pu$ in the source with two cutoff lines at 43. keV and 44.7 keV

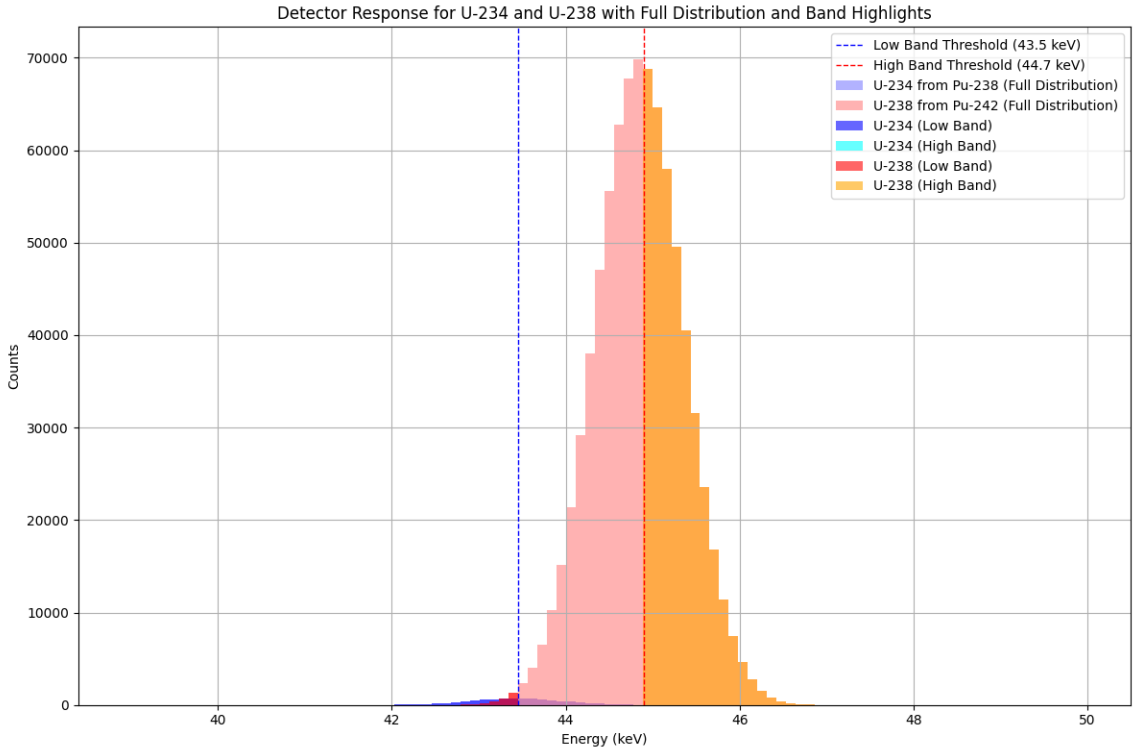


Figure 4-8: Energy distribution for 20% of $^{235}U$ using 20% $^{242}Pu$ in the source with two cutoff lines at 43. keV and 44.7 keV

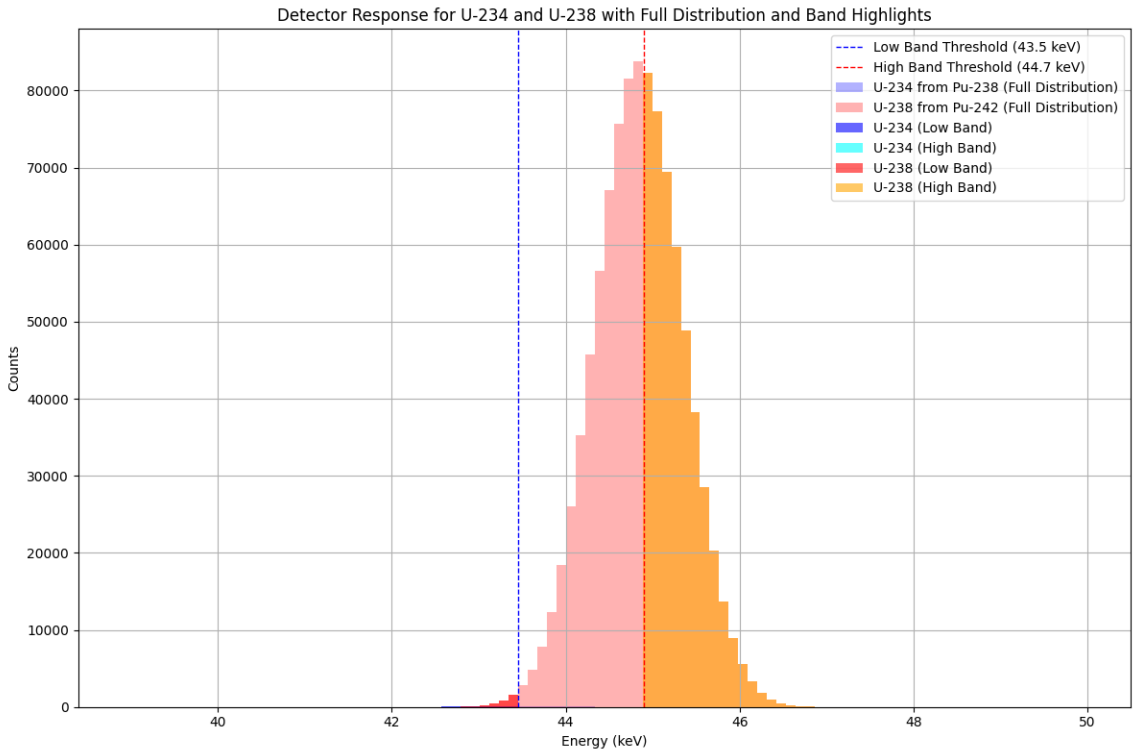


Figure 4-9: Energy distribution for 4% of $^{235}U$ using 20% $^{242}Pu$ in the source with two cutoff lines at 43. keV and 44.7 keV

Table 4-7: Data considering two cutoff lines at 43.5 keV(Low band) and 44.7 keV (High band) for 100% of $^{242}Pu$ activity

| Enrichment [%] | Total Counts U234 - Low band | Total Counts U234 - high band | Total Counts U238 - low band | Total Counts U238 - high band | Ratio Low band/High band | Absolut Uncertainty | Relative Uncertainty |
|---|---|---|---|---|---|---|---|
| **93%** | 26626 | 131 | 956 | 133486 | 0.19902263 | 0.03591816 | 3.34038926 |
| **50%** | 11351 | 41 | 8372 | 1182775 | 0.00956389 | 0.73755616 | 36.8778082 |
| **45%** | 10083 | 47 | 9186 | 1303812 | 0.00771517 | 0.91103838 | 40.9967272 |
| **40%** | 8414 | 34 | 10230 | 1426148 | 0.00588146 | 1.21583076 | 48.6332303 |
| **35%** | 7217 | 32 | 10910 | 1549132 | 0.00464667 | 1.51170847 | 52.9097963 |
| **30%** | 6076 | 27 | 11583 | 1670132 | 0.00362903 | 1.90635286 | 57.1905859 |
| **25%** | 5098 | 17 | 12677 | 1790894 | 0.00283604 | 2.48666144 | 62.1665359 |

| | | | | | | | |
|---|---|---|---|---|---|---|---|
| **20%** | 4190 | 15 | 13532 | 1910915 | 0.00218504 | 3.22959427 | 64.5918854 |
| **4%** | 854 | 2 | 16330 | 2299731 | 0.00036959 | 19.1217799 | 76.4871194 |
| **0.90%** | 240 | 0 | 16921 | 2374670 | 0.00010035 | 70.5041667 | 63.45375 |
| **0.70%** | 143 | 0 | 16948 | 2379718 | 5.9666E-05 | 118.517483 | 84.2659301 |
| **0.20%** | 80 | 0 | 16886 | 2394673 | 3.3174E-05 | 211.075 | 42.215 |

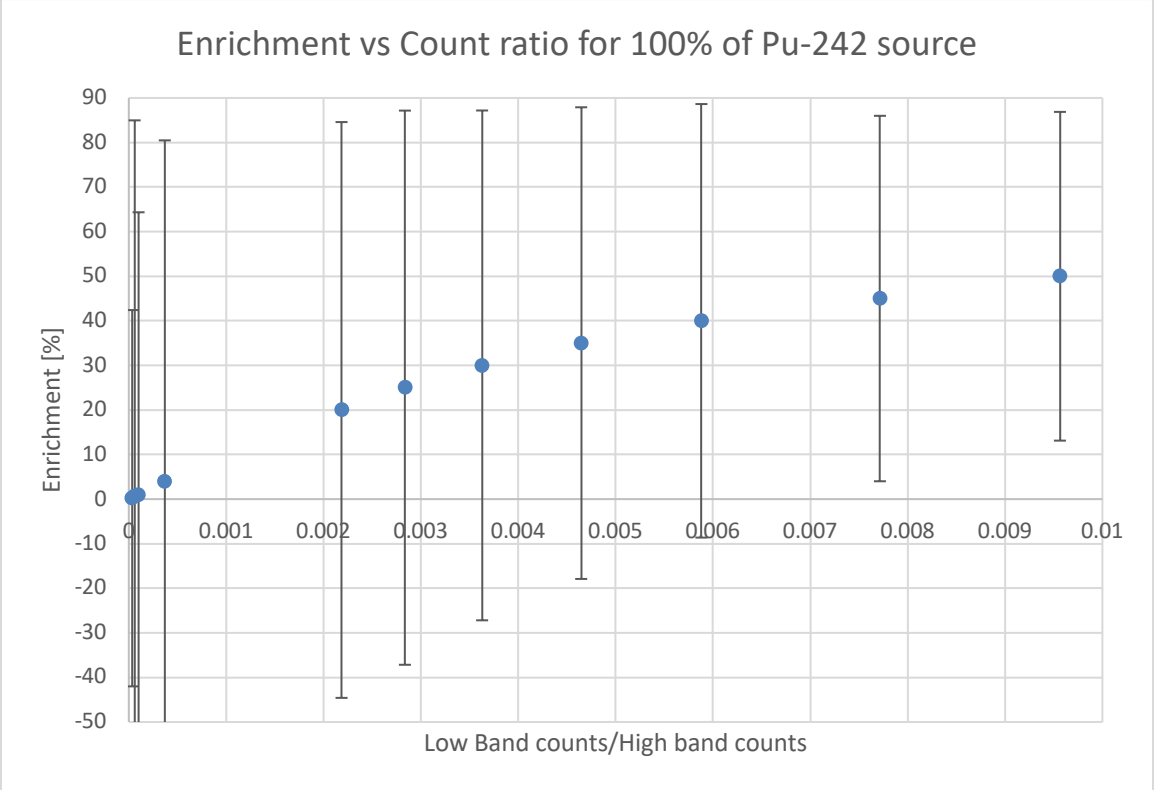


Figure 4-10: Data plotted using two cutoff lines at 43.5 keV and 44.7 keV for 100% of $^{242}$Pu activity

Table 4-8: Data considering two cutoff lines at 43.5 keV(Low band) and 44.7 keV (High band) for 80% of $^{242}Pu$ activity

| Enrichment [%] | Total Counts U234 - Low band | Total Counts U234 - high band | Total Counts U238 - low band | Total Counts U238 - high band | Ratio Low band/High band | Absolut Uncertainty | Relative Uncertainty |
|---|---|---|---|---|---|---|---|
| **93%** | 26664 | 122 | 734 | 106838 | 0.24900532 | 0.02755143 | 2.56228274 |
| **50%** | 11322 | 52 | 6737 | 946994 | 0.01192579 | 0.59503622 | 29.7518108 |
| **45%** | 10074 | 42 | 7330 | 1042220 | 0.00963842 | 0.72761565 | 32.742704 |
| **40%** | 8321 | 30 | 8103 | 1140408 | 0.00727115 | 0.97380123 | 38.952049 |
| **35%** | 7144 | 36 | 8836 | 1239081 | 0.00575359 | 1.23684211 | 43.2894737 |
| **30%** | 6002 | 26 | 9428 | 1335346 | 0.00448254 | 1.57080973 | 47.1242919 |
| **25%** | 4986 | 30 | 10156 | 1432693 | 0.00347646 | 2.03690333 | 50.9225832 |
| **20%** | 4241 | 15 | 10680 | 1529938 | 0.00276253 | 2.51827399 | 50.3654798 |
| **4%** | 881 | 3 | 13150 | 1839901 | 0.00047705 | 14.9262202 | 59.7048808 |
| **0.90%** | 243 | 1 | 13412 | 1900332 | 0.0001275 | 55.1934156 | 49.6740741 |
| **0.70%** | 142 | 0 | 13393 | 1904290 | 7.4048E-05 | 94.3169014 | 67.0593169 |
| **0.20%** | 85 | 0 | 13564 | 1913625 | 4.4106E-05 | 159.576471 | 31.9152941 |

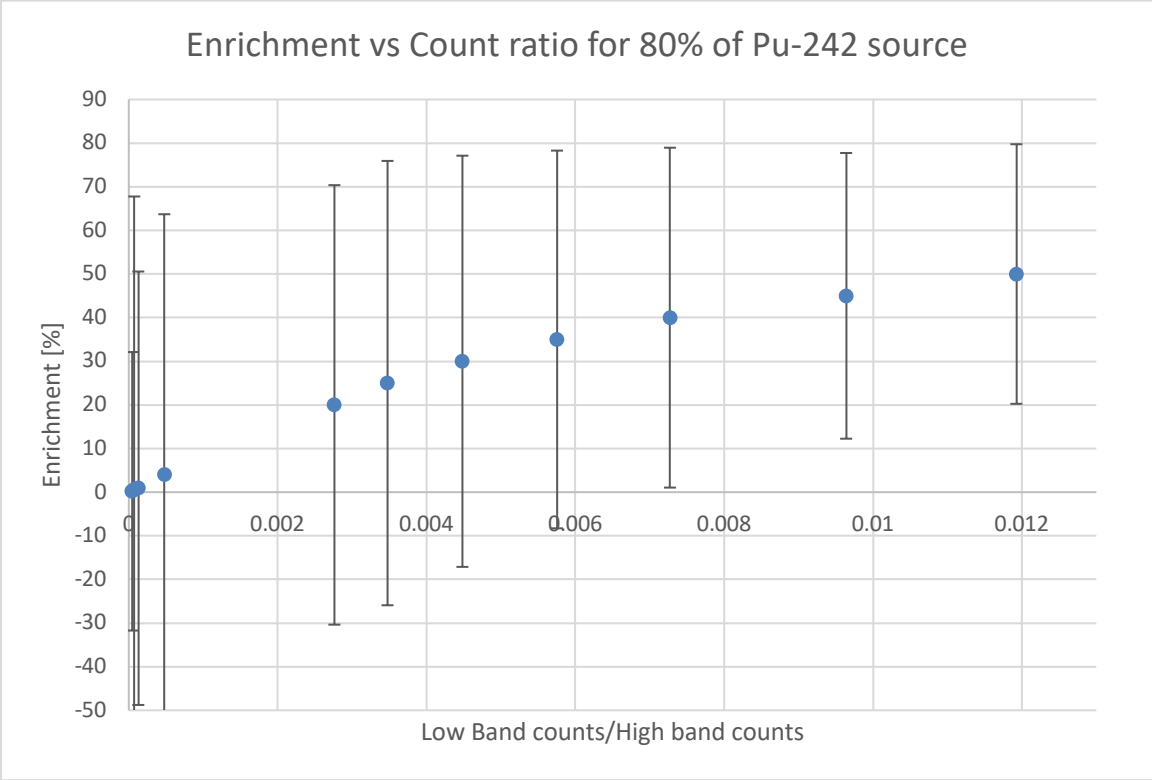


Figure 4-11: Data plotted using two cutoff lines at 43.5 keV and 44.7 keV for 80% of $^{242}$Pu activity

Table 4-9: Data considering two cutoff lines at 43.5 keV(Low band) and 44.7 keV (High band) for 60% of $^{242}$Pu activity

| Enrichment [%] | Total Counts U234 - Low band | Total Counts U234 - high band | Total Counts U238 - low band | Total Counts U238 - high band | Ratio Low band/High band | Absolut Uncertainty | Relative Uncertainty |
|---|---|---|---|---|---|---|---|
| **93%** | 26538 | 131 | 587 | 79929 | 0.33122609 | 0.02217986 | 2.06272721 |
| **50%** | 11277 | 52 | 5021 | 710605 | 0.01583089 | 0.44524254 | 22.2621268 |
| **45%** | 10071 | 40 | 5567 | 782488 | 0.01283032 | 0.5527753 | 24.8748884 |
| **40%** | 8566 | 37 | 6059 | 856230 | 0.00997693 | 0.70733131 | 28.2932524 |
| **35%** | 7064 | 31 | 6552 | 928228 | 0.00759002 | 0.92751982 | 32.4631937 |
| **30%** | 6116 | 25 | 7038 | 1001892 | 0.00608665 | 1.15075213 | 34.5225638 |
| **25%** | 5148 | 19 | 7576 | 1074432 | 0.00477538 | 1.47163947 | 36.7909868 |

| | | | | | | | |
|---|---|---|---|---|---|---|---|
| **20%** | 4209 | 16 | 8054 | 1147483 | 0.00365631 | 1.91351865 | 38.270373 |
| **4%** | 876 | 0 | 9761 | 1381913 | 0.00062946 | 11.1426941 | 44.5707763 |
| **0.90%** | 239 | 0 | 10118 | 1425022 | 0.00016653 | 42.334728 | 38.1012552 |
| **0.70%** | 150 | 0 | 10213 | 1429660 | 0.00010418 | 68.0866667 | 48.40962 |
| **0.20%** | 85 | 0 | 10119 | 1435772 | 5.8787E-05 | 119.047059 | 23.8094118 |

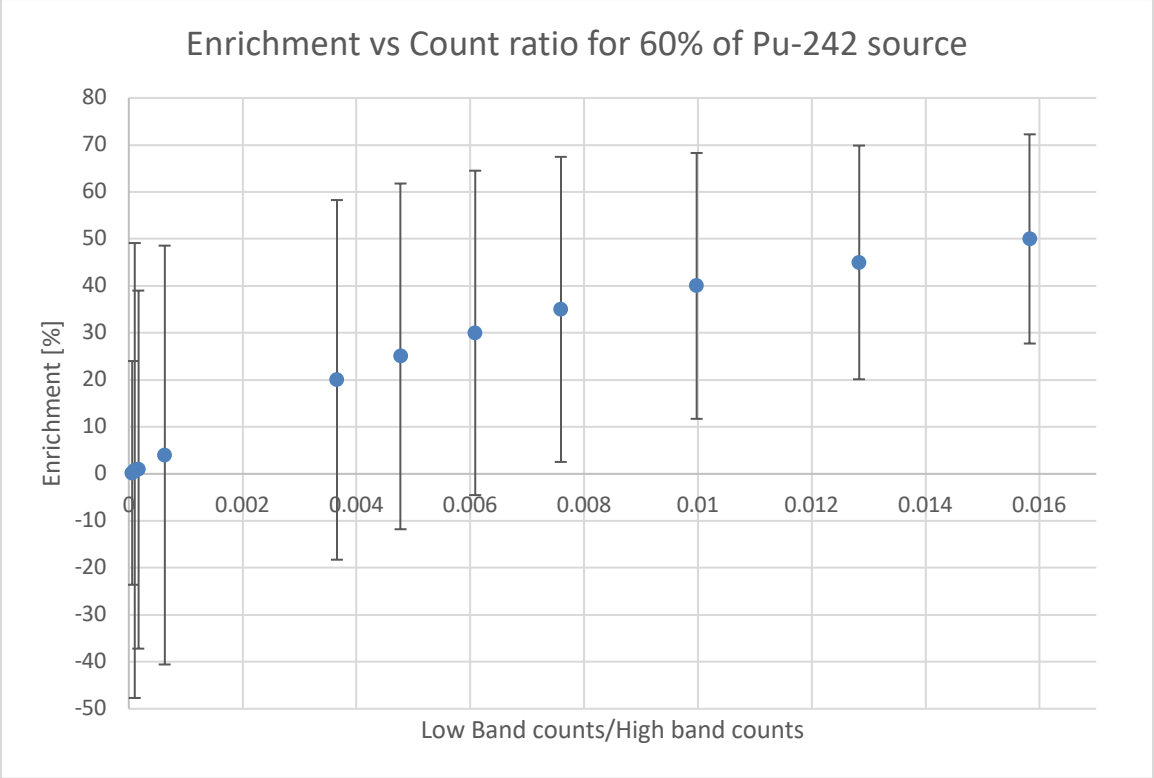


Figure 4-12: Data plotted using two cutoff lines at 43.5 keV and 44.7 keV for 60% of $^{242}$Pu activity

Table 4-10: Data considering two cutoff lines at 43.5 keV(Low band) and 44.7 keV (High band) for 40% of $^{242}Pu$ activity

| Enrichment [%] | Total Counts U234 - Low band | Total Counts U234 - high band | Total Counts U238 - low band | Total Counts U238 - high band | Ratio Low band/High band | Absolut Uncertainty | Relative Uncertainty |
|---|---|---|---|---|---|---|---|
| **93%** | 26549 | 140 | 387 | 53078 | 0.49918638 | 0.01481353 | 1.37765859 |
| **50%** | 11109 | 50 | 3365 | 472858 | 0.0234323 | 0.30290757 | 15.1453785 |
| **45%** | 10020 | 53 | 3676 | 521208 | 0.01919091 | 0.36686628 | 16.5089827 |
| **40%** | 8460 | 38 | 4050 | 570299 | 0.01479588 | 0.47872341 | 19.1489364 |
| **35%** | 7195 | 29 | 4303 | 619739 | 0.01157614 | 0.59805421 | 20.9318972 |
| **30%** | 6083 | 27 | 4754 | 667361 | 0.00909071 | 0.78152228 | 23.4456683 |
| **25%** | 5015 | 14 | 5054 | 716452 | 0.00697014 | 1.00777667 | 25.1944168 |
| **20%** | 4245 | 21 | 5351 | 765177 | 0.00553646 | 1.26054181 | 25.2108363 |
| **4%** | 859 | 3 | 6501 | 919638 | 0.00093075 | 7.56810244 | 30.2724098 |
| **0.90%** | 218 | 0 | 6728 | 950284 | 0.00022779 | 30.8623853 | 27.7761468 |
| **0.70%** | 147 | 0 | 6669 | 952555 | 0.00015325 | 45.3673469 | 32.2561837 |
| **0.20%** | 84 | 0 | 6805 | 957293 | 8.7128E-05 | 81.0119048 | 16.202381 |

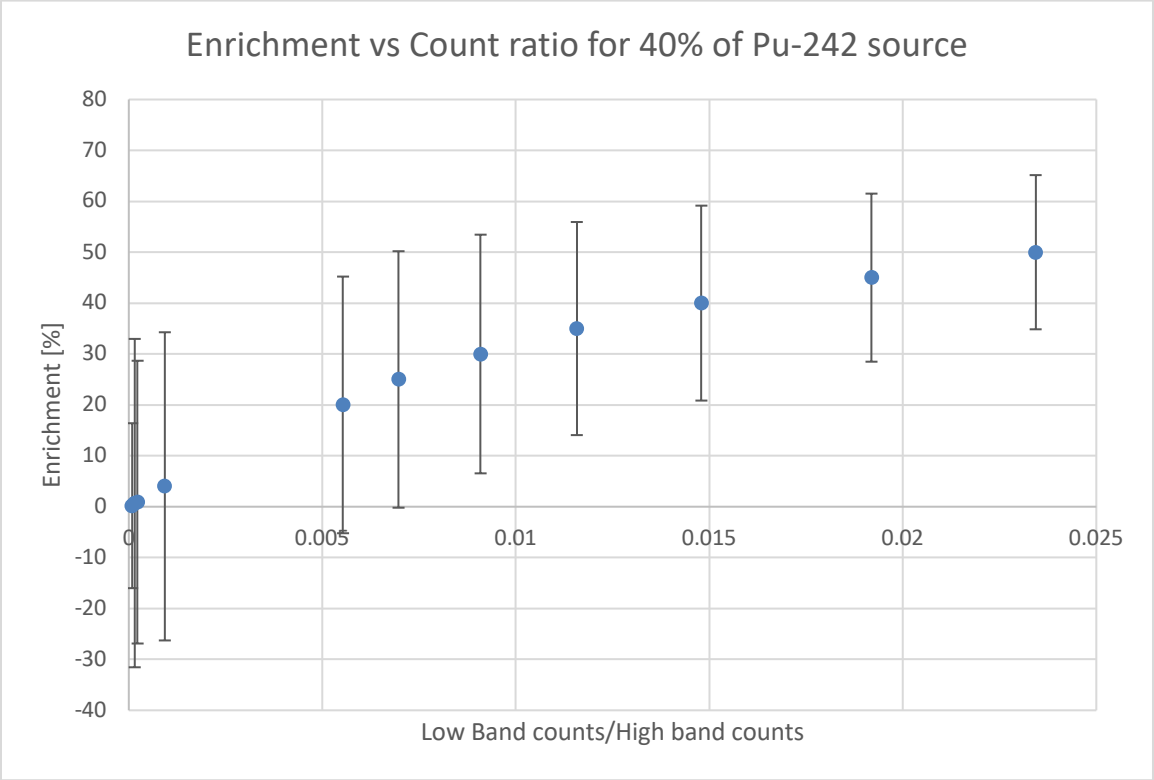


Figure 4-13: Data plotted using two cutoff lines at 43.5 keV and 44.7 keV for 40% of $^{242}$Pu activity

Table 4-11: Data considering two cutoff lines at 43.5 keV(Low band) and 44.7 keV (High band) for 20% of $^{242}$Pu activity

| Enrichment [%] | Total Counts U234 - Low band | Total Counts U234 - high band | Total Counts U238 - low band | Total Counts U238 - high band | Ratio Low band/High band | Absolut Uncertainty | Relative Uncertainty |
|---|---|---|---|---|---|---|---|
| **93%** | 26614 | 133 | 184 | 26885 | 0.98810447 | 0.00850126 | 0.79061702 |
| **50%** | 11190 | 51 | 1654 | 236411 | 0.0472182 | 0.1478107 | 7.39053513 |
| **45%** | 10147 | 42 | 1915 | 260679 | 0.03880134 | 0.1887258 | 8.49266102 |
| **40%** | 8429 | 36 | 1949 | 284768 | 0.02952389 | 0.23122557 | 9.24902262 |
| **35%** | 7224 | 22 | 2148 | 310454 | 0.02317963 | 0.2973422 | 10.406977 |
| **30%** | 6125 | 27 | 2328 | 333495 | 0.01831917 | 0.38008164 | 11.4024492 |
| **25%** | 5101 | 21 | 2435 | 357961 | 0.01421214 | 0.47735738 | 11.9339346 |
| **20%** | 4178 | 26 | 2686 | 382304 | 0.01091976 | 0.64289134 | 12.8578268 |

| | | | | | | | |
|---|---|---|---|---|---|---|---|
| **4%** | 877 | 6 | 3130 | 459528 | 0.00190854 | 3.56898518 | 14.2759407 |
| **0.90%** | 229 | 0 | 3389 | 475050 | 0.00047864 | 14.7991266 | 13.319214 |
| **0.70%** | 134 | 0 | 3451 | 475570 | 0.00027974 | 25.7537313 | 18.310903 |
| **0.20%** | 86 | 0 | 3335 | 478408 | 0.00017852 | 38.7790698 | 7.75581395 |

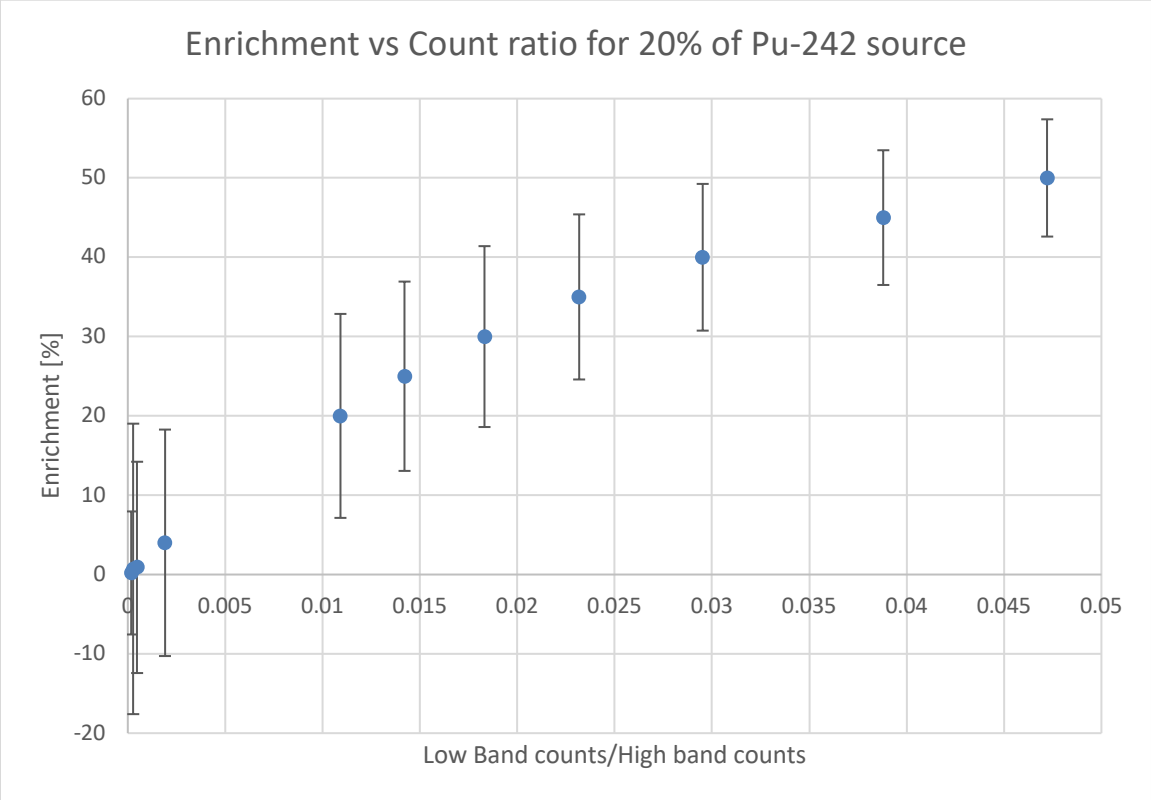


Figure 4-14: Data plotted using two cutoff lines at 43.5 keV and 44.7 keV for 20% of $^{242}$Pu activity

Table 4-12: Data considering two cutoff lines at 43.5 keV(Low band) and 44.7 keV (High band) for 10% of $^{242}$Pu activity

| **Enrichment [%]** | **Total Counts U234 - Low band** | **Total Counts U234 - high band** | **Total Counts U238 - low band** | **Total Counts U238 - high band** | **Ratio Low band/High band** | **Absolut Uncertainty** | **Relative Uncertainty** |
|---|---|---|---|---|---|---|---|
| **93%** | 26512 | 129 | 90 | 13295 | 1.99036235 | 0.0102796 | 0.95600247 |

| | | | | | | | |
|---|---|---|---|---|---|---|---|
| **50%** | 11148 | 52 | 835 | 118463 | 0.09388255 | 0.07490261 | 3.74513069 |
| **45%** | 10076 | 41 | 940 | 130463 | 0.07699215 | 0.09329152 | 4.1981183 |
| **40%** | 8404 | 37 | 986 | 142958 | 0.05864086 | 0.11732537 | 4.69301475 |
| **35%** | 7145 | 35 | 1084 | 154635 | 0.0461087 | 0.15171465 | 5.31001291 |
| **30%** | 6125 | 28 | 1163 | 167278 | 0.03652911 | 0.18987762 | 5.69632874 |
| **25%** | 5045 | 19 | 1263 | 178957 | 0.02809899 | 0.2503469 | 6.25867252 |
| **20%** | 4167 | 23 | 1323 | 191660 | 0.02171176 | 0.31749462 | 6.34989246 |
| **4%** | 881 | 1 | 1678 | 230125 | 0.00380496 | 1.9046538 | 7.61861521 |
| **0.90%** | 258 | 0 | 1625 | 238066 | 0.00107639 | 6.29844961 | 5.66860465 |
| **0.70%** | 140 | 0 | 1730 | 238304 | 0.00058325 | 12.3571429 | 8.78592857 |
| **0.20%** | 89 | 0 | 1735 | 239632 | 0.00036873 | 19.494382 | 3.8988764 |

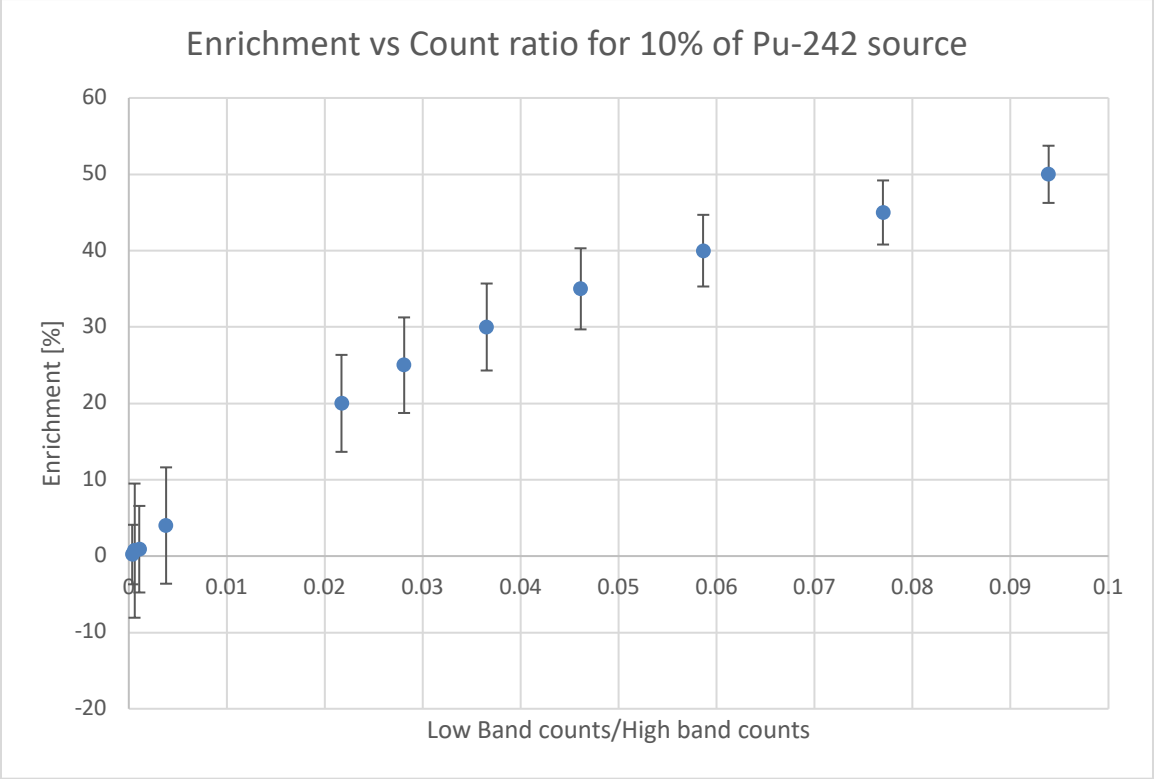


Figure 4-15: Data plotted using two cutoff lines at 43.5 keV and 44.7 keV for 10% of $^{242}$Pu activity

Figure 4-15 and Table 4-12 indicate that $^{234}U$ and $^{238}U$ Mossbauer array should be able to differentiate between High Enriched Uranium samples of >30% $^{235}U$ from that of Low Enriched material (i.e., <20% $^{235}U$).

# Chapter 5

# Conclusion

Model simulations were used to investigate the feasibility of using Mossbauer spectroscopy for detecting the presence of HEU in environmental samples as a tool for proliferation detection. The detection of HEU by MS exploits the relationship between the relative abundance of $^{234}U$ (measured as a ratio relative to $^{238}U$ abundance) and that of the $^{235}U$, since $^{235}U$ is not Mossbauer active. The effect of changing three main variables on the detection of HEU were explored including detector resolution, source activity and various methods of energy gating. Of these variables, detector resolution was found to be most important to the performance of UxMS. However, differentiating HEU from LEU was not possible, even when using a detector with 1% energy resolution.

Due to the natural abundance differences between $^{238}U$ and $^{234}U$, adjusting the relative source strengths of the parent isotopes $^{238}Pu$ and $^{242}Pu$, respectively, also had a positive effect on performance of UxMS. Decreasing the $^{242}Pu$ source activity by an order of magnitude, relative to the $^{238}Pu$ activity, measurement uncertainties of the enrichment of U-bearing materials decreased by mor than an order of magnitude. Even so, this was not sufficient to differentiate between HEU and LEU at any enrichment.

Finally, a novel two-point energy cutoff method was used to separate counts from $^{234}U$ and $^{238}U$. When coupled with a high resolution detector (1% FWHM) and a 1:10 mixed radioactive source of $^{238}Pu$:$^{242}Pu$, UxMAS was able to differentiate between LEU and HEU with high confidence at $^{235}U$ enrichment levels of ~25-30%.

# Chapter 6

## Future Work

For future developments, one promising direction is the implementation of a system with two synchronized velocity transducer s to drive two separate sources simultaneously. This set up would enable the measurement of resonant gamma-ray emission from a sample containing two different isotopes at the same time, providing insights into their interactions and contributions to the observed spectrum.

Additionally, constructing an experimental setup capable of performing the measurements and analysis discussed in this thesis could further validate the approach. Such a setup would facilitate evaluating the reliability and accuracy of this technique for identifying and quantifying uranium isotopes in a sample. This would advance the use of Mössbauer spectroscopy as non-destructive method for isotope analysis, particularly in applications related to non-proliferation efforts, where precision and minimal material alteration are crucial.

# References

[1] Moody, K. J., & Lawrence Livermore National Lab., CA (United States), Dissolved Oralloy standards and the origin of HEU, (1994).
[2] DOE Occupational Radiation Exposure, 1995.
[3] Royal Society of Chemistry, Mossbauer Spectroscopy Group, Introduction to Mössbauer Spectroscopy, (2024).
[4] Filatov, M., On the Calculation of Mössbauer isomer shift, The Journal of Chemical Physics, 127, 084101, (2007).
[5] Long, G., J., Grandjean, F., Mössbauer Spectroscopy applied to Magnetism and Materials Science, vol1, (1993).
[6] Kistner, O. C., and Sunyar, A. W., Phys. Rev. Lett. 4, 212 (1960).
[7] Pound, R. V. and Rebka, Jr., G. A. Phys Rev. Lett. 4, 274 (1960), and Joseph-son, B. D., ibid. 4, 341 (1960).
[8] Bland, J., A Mössbauer Spectroscopy and Magnetometry Study of magnetic Multilayers and Oxides, Oliver Lodge Laboratory, University of Liverpool, (2002).
[9] J.R.Haskins, Advanced Mössbauer-Effect experiments, (1964).
[10] MacDow, K., Libre texts Chemistry, Mossbauer Spectroscopy.
[11] Dickson, D. P. E. and Berry, F. J., Mössbauer Spectroscopy, Cambridge University Press (1986)
[12] Greenwood, N. N., and Gibb, T. C., Mössbauer Spectroscopy, Chapman and Hall Ltd, London, (1971).
[13] Cohen, R. L., ed. (1976 and 1980). Applications of Mössbauer Spectroscopy, Vols. I and II, Academic Press, New York.
[14] Gibb, T. C. (1977). Principles of Mössbauer Spectroscopy, Chapman and Hall, London.
[15] Gonser, U, ed (1975) Topics in Applied Physics, Vol. V: Mössbauer Spectroscopy, Springer-Verlag, Berlin.
[16] Gonser, U., ed. (1981). Mössbauer Spectroscopy II: The Exotic Side of the Method, Springer-Verlag, Berlin.
[17] Sternheimer, R. M., Quadrupole Antishielding Factors of Ions, Phys. Rev. 132, 1637 American Physical Society, (1963).
[18] Parish, R. V., Johnson, C. E., The origin of the Quadrupole Splitting in the Mössbauer Spectra of some organotin Halide complexes, Chemical Physics Letters, Vol. 6, no. 3, (1970).
[19] Goodman, B. A., Mössbauer spectroscopy, Department of spectrochemistry, Scotland, (1982)
[20] Gruverman, I. J., ed. (1965-74). Mössbauer Effect Methodology, Vols. I-IX, Plenum Press, New York.
[21] Long, G. J., ed. (1984). Mössbauer Spectroscopy Applied to Inorganic Chemistry, Vol. 1, Plenum Press, New York.
[22] May, L. (1971). An Introduction to Mössbauer Spectroscopy, Plenum Press, New York.
[23] Mössbauer, R. L. (1958). Z. Physik, 151, 124.

[24] Thosar, B. V., Srivastava, J. K., lyengar, P. K. & Bhargava, S. C., eds. (1983). [20] Advances in Mössbauer Spectroscopy, Applications to Physics, Chemistry and Biology, Elsevier, Amsterdam and New York.
[25] Wertheim, G. K. (1964). Mössbauer Effect Principles and Applications, Academic Press, New York.
[26] Poetzel, W., Moser, J., Asch .L., and Kalvius, V. M., Mössbauer Spectroscopy with Actinides Elements, Hyperfine interactions 13 (1983)175-198, (1982)
[27] Freeman, A. J., Darby, Jr., J. B., The actinides: Electronic Structure and related properties, Vol. I and II, Academic Press, New York, (1974).
[28] Brodsky, M. B., Trainor, R. J. Physica 86-88B (1977) 143.
[29] Brodsky, M. B., Trainor, R. J. Physica 91B (1977) 271.
[30] Brodsky, M. B., Rep. Prog. Phys. 41 (1978) 1547.
[31] Monard, J. A., Huray, P. G., Thomson, J. O. – Mossbauer studies of electric hyperfine interactions in $^{234U}$, $^{236}$U and $^{238}$U, Oak Ridge National Laboratory, Oak Ridge, Tennessee, (1974).
[32] Meeker, R., D., Kalvius, G., M., Dunlap, B., D., et. al. – Hyperfine interactions and nuclear moments in even uranium isotopes from Mössbauer spectroscopy, Nuclear Physics A224 (1974) 429-436.
[33] Brugge, D., Uranium, Encyclopedia of Toxicology (Third Edition) (2014) 883-884.
[34] Kalvius, G., M., - Mossbauer Spectroscopy of Actinides: some application to solid state chemistry, Journal of Less- Common Metals, 121 (1986) 353-378
[35] Ruby, S., L., Kalvius, G., M., Dunlap, B., D., et. al. – Nuclear Gamma-ray resonance study of Hyperfine interactions in $^{238}$U, Physical review 2 184 (1969)
[36] Jové, J., He, L., Proust, J., and Pagès, M., - Mössbauer spectroscopy as a nuclear probe for solid state transuranium chemistry, Journal of Alloys and Compounds, 177 (1991) 285-310
[37] Knauer, R. C., and Mullen J. G., Rev. Sci. Instr. 1967, 38, 1624.
[38] Eisen, Y., Shor, A., CdTe and CdZnTe materials for room-temperatures X-ray and gamma ray detectors, Journal of crystal growth 184/185 (1998) 1302-1312.
[39] Richter, M., Stiffer, P., High resolution gamma ray spectroscopy with CdTe detectors systems, Nuclear Instruments and Methods in Physics Research A322 (1992) 529-537.
[40] Abbaspour, S,. Mahmoudian, B., Islamian. J., P., Cadmium Telluride Semiconductor Detector for Improved Spatial and Energy Resolution Radioisotopic Imaging, World J Nucl Med, 2017; 16:101-7.
[41] Tanaka, T., Kobayashi, Y., Mitani, T., et. al., Recent achievements of the high resolution Shottky CdTe diode for γ-ray detectors. New Astronomy Reviews 48 (2004) 309-313.
[42] AmpTek/Ametek®, CdTe X-Ray & Gamma Ray Detector description.
[43] Perez-Andujar, A., Pibida, L., Performance of CdTe, HpGe and NaI(Tl) detectors for radioactivity measurements, Applied Radiation and Isotopes 60 (2004) 41-47.
[44] Hossain, I., Sharip, N., Viswanathan, K. K., Efficiency and resolution of HPGe and NaI(Tl) detectors using gamma-ray spectroscopy. Scientific Research and Essays Vol. 7(1), pp. 86-89, 2012.
[45] Mirion Technologies®, Detectors Flanged$^{TM}$ Cryostats, Liquid Nitrogen Cryostat.
[46] Bortels, G., et. al., Alpha-Particle and Photon Emission Probabilities in the $^{238}$Pu-$^{234}$U Decay, Nuclear Instruments and Methods, 1984.
[47] National Nuclear Data Center (NNDC), "Evaluated Nuclear Structure Data File (ENSDF)," Brookhaven National Laboratory, Available at: https://www.nndc.bnl.gov, accessed in November 2024.
[48] Sharma, V. K., Klingelhofer, G., Nishida, T., Mössbauer Spectroscopy: Applications in chemistry, biology and nanotechnology. John Wiley & Sons. (2013)

## Appendix A

# Mössbauer Transition in Actinide Isotopes table

Table A: Important parameters for Mössbauer transition in actinides isotopes [48]

| Isotopes | Eγ (keV) | $N_a$ (%) | $I_{ex}$ | $I_{gd}$ | $t_{1/2}$ (ns) | Γ (mm $s^{-1}$) | $t_s$ | Source |
|---|---|---|---|---|---|---|---|---|
| **$^{232}$Th** | 49.8 | 100 | 2 | 0 | 0.2 | 43 | 119 s | $^{232}$Ac |
| **$^{231}$Pa** | 84.21 | – | 3/2 | 5/2 | 44 | 0.08 | 25.5 h | $^{231}$Th |
| **$^{234}$U** | 43.49 | 0.005 | 2 | 0 | 0.25 | 24 | 86 years | $^{238}$Pu |
| **$^{236}$U** | 45.24 | – | 2 | 0 | 0.23 | 26 | $6.58 \times 10^3$ years | $^{240}$Pu |
| **$^{238}$U** | 44.91 | 99.275 | 2 | 0 | 0.21 | 27 | $3.79 \times 10^5$ years | $^{242}$Pu |
| **$^{237}$Np** | 59.536 | – | 5/2 | 5/2 | 68 | 0.07 | 458 years | $^{241}$Am |
| **$^{239}$Pu** | 57.273 | – | 5/2 | 1/2 | 0.10 | 47.9 | 2.33 days | $^{239}$Np |
| **$^{243}$Am** | 84.0 | – | 5/2 | 5/2 | 2.3 | 1.4 | 4.98 h | $^{243}$Pu |

Where, Eγ is the transition energy of the Mössbauer effect; $N_a$ means the natural abundance; $I_{ex}$ is the nuclear spin of the excited state in the Mössbauer transition; $I_{gd}$ equates the nuclear spin of the ground state in the Mössbauer transition; $t_{1/2}$ is the half-life of the excited state in the Mössbauer transition; Γ is the natural linewidth; and $t_s$ is the lifetime of the isotopes for the Mössbauer source [48].

**Appendix B**

## Simulation code for all approaches

```
import numpy as np
import matplotlib.pyplot as plt

def simulate_gaussian_distribution(activity, fraction, half_life, measurement_time,
E_gamma, linewidth):
    # Convert activity from micro Curie to decays per second (Bq)
    activity_bq = activity * 3.7e4  # 1 micro Curie = 3.7e4 decays per second

    # Decay constant
    lambda_decay = np.log(2) / half_life

    # Calculate the Decay rate
    N_decays = activity_bq * measurement_time

    # Number of gamma-ray emissions
    N_gamma = N_decays * fraction

    # Limit the number of samples to avoid memory issues
    N_gamma = min(N_gamma, 10**6)

    # Gaussian distribution for the energy spectrum
    energies = np.random.normal(E_gamma, linewidth, int(N_gamma))

    return energies

def simulate_detector_response(energies, num_channels, energy_range):
    hist, bin_edges = np.histogram(energies, bins=num_channels, range=energy_range)
    return hist, bin_edges

# Parameters for U-234 from Pu-238
activity_pu238 = 100                # in micro Curie
fraction_pu238 = 0.000392               # fraction of 43.5 keV gamma-ray emission
(0.0392%)
half_life_pu238 = 87.7 * 365.25 * 24 * 3600  # in seconds (87.7 years)
E_gamma_u234 = 43.5                     # in keV, specific gamma-ray energy for U-234
from Pu-238
linewidth_u234 = 0.5                # in keV (adjusted for better visualization)

# Parameters for U-238 from Pu-242
```

```
activity_pu242 = 100                    # in micro Curie
fraction_pu242 = 0.000384               # fraction of 44.7 keV gamma-ray emission
(0.0384%)
half_life_pu242 = 3.73e5 * 365.25 * 24 * 3600  # in seconds (373,000 years)
E_gamma_u238 = 44.7                     # in keV, specific gamma-ray energy for U-238
from Pu-242
linewidth_u238 = 0.5                    # in keV (adjusted for better visualization)

# Measurement time in seconds
measurement_time = 1 * 3600             # in seconds (1 hour)

# Detector parameters
num_channels = 100                      # number of channels for the histogram
energy_range = (39, 50)                 # energy range in keV

# Simulate energy distributions for U-234 and U-238
energies_u234 = simulate_gaussian_distribution(activity_pu238, fraction_pu238,
half_life_pu238, measurement_time, E_gamma_u234, linewidth_u234)
energies_u238 = simulate_gaussian_distribution(activity_pu242, fraction_pu242,
half_life_pu242, measurement_time, E_gamma_u238, linewidth_u238)

# Simulate detector response for U-234
hist_u234, bin_edges_u234 = simulate_detector_response(energies_u234, num_channels,
energy_range)

# Simulate detector response for U-238
hist_u238, bin_edges_u238 = simulate_detector_response(energies_u238, num_channels,
energy_range)

# Plot detector response for both isotopes
plt.figure(figsize=(8, 6))

plt.bar(bin_edges_u234[:-1], hist_u234, width=np.diff(bin_edges_u234), color='blue',
alpha=0.5, label='U-234 from Pu-238')
plt.bar(bin_edges_u238[:-1], hist_u238, width=np.diff(bin_edges_u238), color='red',
alpha=0.5, label='U-238 from Pu-242')

plt.title('Gaussian distribution of the source')
plt.xlabel('Energy (keV)')
plt.ylabel('Counts')
plt.grid()
plt.legend()

plt.tight_layout()
plt.show()
```

```
## ----------------------------- ##

import numpy as np
import matplotlib.pyplot as plt

def simulate_gaussian_distribution_with_velocity(activity, fraction, half_life,
measurement_time, E_gamma, linewidth, velocities):
    c = 3e8  # Speed of light in meters per second
    N_gamma = activity * 3.7e4 * measurement_time * fraction  # Convert activity to total
gamma emissions

    total_counts = []

    for velocity in velocities:
        delta_E = (velocity / 1000 / c) * E_gamma  # Doppler shift
        counts = N_gamma  # The number of counts is the same as the number of gamma
emissions
        total_counts.append(counts)

    return velocities, total_counts

# Parameters for U-234 from Pu-238
activity_pu238 = 100                # in micro Curie
fraction_pu238 = 0.000392               # fraction of 43.5 keV gamma-ray emission
(0.0392%)
half_life_pu238 = 87.7 * 365.25 * 24 * 3600  # in seconds (87.7 years)
E_gamma_u234 = 43.5                   # in keV, specific gamma-ray energy for U-234
from Pu-238
linewidth_u234 = 0.5                # in keV (adjusted for better visualization)

# Parameters for U-238 from Pu-242
activity_pu242 = 100                # in micro Curie
fraction_pu242 = 0.000384               # fraction of 44.9 keV gamma-ray emission
(0.0384%)
half_life_pu242 = 3.73e5 * 365.25 * 24 * 3600  # in seconds (373,000 years)
E_gamma_u238 = 44.7                   # in keV, specific gamma-ray energy for U-238
from Pu-242
linewidth_u238 = 0.5                # in keV (adjusted for better visualization)

# Measurement time in seconds
measurement_time = 1 * 3600             # in seconds (1 hour)

# Detector parameters
velocities = np.linspace(-20, 20, 100)    # Simulate a range of velocities in mm/s
```

```
# Simulate counts vs velocity for U-234
velocities, counts_u234 = simulate_gaussian_distribution_with_velocity(activity_pu238, fraction_pu238, half_life_pu238, measurement_time, E_gamma_u234, linewidth_u234, velocities)

# Simulate counts vs velocity for U-238
_, counts_u238 = simulate_gaussian_distribution_with_velocity(activity_pu242, fraction_pu242, half_life_pu242, measurement_time, E_gamma_u238, linewidth_u238, velocities)

# Sum the counts from both isotopes
total_counts = np.array(counts_u234) + np.array(counts_u238)

# Plot total counts vs velocity
plt.figure(figsize=(8, 6))

plt.plot(velocities, total_counts,'bo-', label='Total Counts')
plt.title('Total Counts vs Velocity for U-234 and U-238')
plt.xlabel('Velocity (mm/s)')
plt.ylabel('Total Counts')
plt.grid()
plt.legend()

plt.tight_layout()
plt.show()

## ------------------------ ##

import numpy as np
import matplotlib.pyplot as plt
from scipy.ndimage import gaussian_filter1d

def simulate_counts_with_velocity(activity, fraction, half_life, measurement_time, E_gamma, linewidth, velocities):
    c = 3e8  # Speed of light in meters per second
    N_gamma = activity * 3.7e4 * measurement_time * fraction  # Convert activity to total gamma emissions

    counts_per_velocity = []

    for velocity in velocities:
        delta_E = (velocity / 1000 / c) * E_gamma  # Doppler shift
        energies = np.random.normal(E_gamma + delta_E, linewidth, int(N_gamma))
        counts = len(energies)
```

```
        counts_per_velocity.append(counts)

    return velocities, np.array(counts_per_velocity)

# Function to simulate detector response with specified resolution
def simulate_detector_response(counts, resolution):
    smoothed_counts = gaussian_filter1d(counts, sigma=resolution)
    return smoothed_counts

# Parameters for Source U-234 and U-238
activity_pu238_source = 100              # in micro Curie for Pu-238
fraction_pu238_source = 0.000392         # fraction of 43.5 keV gamma-ray emission for
U-234
half_life_pu238_source = 87.7 * 365.25 * 24 * 3600  # in seconds (87.7 years)
E_gamma_u234_source = 43.5               # in keV
linewidth_u234_source = 0.5              # in keV

activity_pu242_source = 100              # in micro Curie for Pu-242
fraction_pu242_source = 0.000384         # fraction of 44.7 keV gamma-ray emission for
U-238
half_life_pu242_source = 3.73e5 * 365.25 * 24 * 3600  # in seconds (373,000 years)
E_gamma_u238_source = 44.7               # in keV
linewidth_u238_source = 0.5              # in keV

# Parameters for Sample U-234 and U-238 (Stationary)
activity_u234_sample = 50                # in micro Curie for U-234 in sample
fraction_u234_sample = 0.000392          # fraction of 43.5 keV gamma-ray emission for
U-234
half_life_u234_sample = 2.46e5 * 365.25 * 24 * 3600  # in seconds (245,500 years)
E_gamma_u234_sample = 43.5               # in keV
linewidth_u234_sample = 0.5              # in keV

activity_u238_sample = 50                # in micro Curie for U-238 in sample
fraction_u238_sample = 0.000384          # fraction of 44.7 keV gamma-ray emission for
U-238
half_life_u238_sample = 4.47e9 * 365.25 * 24 * 3600  # in seconds (4.47 billion years)
E_gamma_u238_sample = 44.7               # in keV
linewidth_u238_sample = 0.5              # in keV

# Measurement time in seconds
measurement_time = 1 * 3600              # in seconds (1 hour)

# Detector parameters
velocities = np.linspace(-20, 20, 100)    # Simulate a range of velocities in mm/s
resolution = 2                           # Resolution of the detector (smoothing factor)
```

```
# Simulate counts vs velocity for Source U-234
velocities, counts_u234_source = simulate_counts_with_velocity(activity_pu238_source,
fraction_pu238_source, half_life_pu238_source, measurement_time,
E_gamma_u234_source, linewidth_u234_source, velocities)

# Simulate counts vs velocity for Source U-238
_, counts_u238_source = simulate_counts_with_velocity(activity_pu242_source,
fraction_pu242_source, half_life_pu242_source, measurement_time,
E_gamma_u238_source, linewidth_u238_source, velocities)

# Sum the counts from the source
total_counts_source = counts_u234_source + counts_u238_source

# Simulate stationary sample response (no velocity dependency)
# The sample's absorption will create a Gaussian drop centered at 0 mm/s
# Here, we simulate the counts that the sample would absorb at 0 mm/s

# Simulate sample counts for U-234
velocities_sample = np.zeros_like(velocities)  # The sample is stationary, so it doesn't
move
_, counts_u234_sample = simulate_counts_with_velocity(activity_u234_sample,
fraction_u234_sample, half_life_u234_sample, measurement_time,
E_gamma_u234_sample, linewidth_u234_sample, velocities_sample)

# Simulate sample counts for U-238
_, counts_u238_sample = simulate_counts_with_velocity(activity_u238_sample,
fraction_u238_sample, half_life_u238_sample, measurement_time,
E_gamma_u238_sample, linewidth_u238_sample, velocities_sample)

# Sum the counts from the sample
total_counts_sample = counts_u234_sample + counts_u238_sample

# Create a Gaussian absorption profile centered at 0 mm/s based on sample's absorption
absorption_profile = np.exp(-((velocities) ** 2) / (2 * linewidth_u234_sample ** 2))
absorption_counts = total_counts_sample[0] * absorption_profile

# Apply the absorption profile to the source counts
final_detected_counts = total_counts_source - absorption_counts

# Apply detector response (smoothing) to the final detected counts
detected_counts_with_absorption = simulate_detector_response(final_detected_counts,
resolution)

# Plot detected counts vs velocity with absorption effect
```

```
plt.figure(figsize=(8, 6))

plt.plot(velocities, detected_counts_with_absorption,'bo-', label='Detected Counts (After Sample Absorption')
plt.title('Detected Counts vs Velocity')
plt.xlabel('Velocity (mm/s)')
plt.ylabel('Detected Counts')
plt.grid()
plt.legend()

plt.tight_layout()
plt.show()

## ---------------------- ##

import numpy as np
import matplotlib.pyplot as plt
from scipy.ndimage import gaussian_filter1d
from mpl_toolkits.mplot3d import Axes3D

def simulate_counts_with_velocity(activity, fraction, half_life, measurement_time, E_gamma, linewidth, velocities):
    c = 3e8  # Speed of light in meters per second
    N_gamma = activity * 3.7e4 * measurement_time * fraction  # Convert activity to total gamma emissions

    counts_per_velocity = []
    energy_levels = np.linspace(43.0, 45.5, 50)  # Fine resolution for energy axis
    energy_distribution = np.ones((len(velocities), len(energy_levels)))  # Start with a flat surface

    for i, velocity in enumerate(velocities):
        for j, energy in enumerate(energy_levels):
            # Apply Gaussian absorption at the resonance energies
            absorption_u234 = np.exp(-((velocity)**2 + (energy - 43.5)**2) / (2 * (linewidth**2))) * 0.2  # Shallower dip
            absorption_u238 = np.exp(-((velocity)**2 + (energy - 44.7)**2) / (2 * (linewidth**2))) * 0.4  # Deeper dip

            energy_distribution[i, j] -= (absorption_u234 + absorption_u238)

    return velocities, energy_levels, energy_distribution

# Parameters
activity_pu238_source = 100
```

```
fraction_pu238_source = 0.000392
half_life_pu238_source = 87.7 * 365.25 * 24 * 3600
linewidth = 0.5

activity_pu242_source = 100
fraction_pu242_source = 0.000384
half_life_pu242_source = 3.73e5 * 365.25 * 24 * 3600

measurement_time = 1 * 3600
velocities = np.linspace(-20, 20, 100)
resolution = 2

# Simulate counts vs velocity for U-234 and U-238
velocities, energy_levels, energy_distribution = simulate_counts_with_velocity(
    activity_pu238_source, fraction_pu238_source, half_life_pu238_source,
measurement_time, 43.5, linewidth, velocities)

# Create 3D surface plot
fig = plt.figure(figsize=(10, 7))
ax = fig.add_subplot(111, projection='3d')
X, Y = np.meshgrid(velocities, energy_levels)
Z = energy_distribution.T  # Transpose to match the dimensions correctly
ax.plot_surface(X, Y, Z, cmap='inferno', edgecolor='none')

ax.set_xlabel('Velocity (mm/s)')
ax.set_ylabel('Gamma-ray Energy (keV)')
ax.set_zlabel('Normalized Detected Counts')
ax.set_title('Mossbauer effect in a function of the gamma-ray energy')

plt.show()

## ---------------------- ##

import numpy as np
import matplotlib.pyplot as plt
from scipy.ndimage import gaussian_filter1d

# Constants
Avogadro = 6.022e23             # Avogadro's number
speed_of_light = 3.0e8          # speed of light in m/s

# Function to simulate Gaussian distribution of gamma-ray energies
def simulate_gaussian_distribution(activity_ci, fraction, half_life, measurement_time,
E_gamma, linewidth):
    activity = activity_ci * 3.7e10
```

```
    lambda_decay = np.log(2) / half_life
    N_decays = activity * measurement_time
    N_gamma = N_decays * fraction
    energies = np.random.normal(E_gamma, linewidth, int(N_gamma))
    return energies

# Function to simulate detector response with specified resolution
def simulate_detector_response(energies, num_channels, energy_range, resolution):
    hist, bin_edges = np.histogram(energies, bins=num_channels, range=energy_range,
density=False)
    smoothed_hist = gaussian_filter1d(hist, sigma=resolution)
    return smoothed_hist, bin_edges

# Parameters for U-234 from Pu-238
activity_pu238_ci = 1e-6            # in curies (100 microCurie)
fraction_pu238 = 0.000392             # fraction of 43.5 keV gamma-ray emission
(0.0392%)
half_life_pu238 = 87.7 * 365.25 * 24 * 3600  # in seconds (87.7 years)
E_gamma_u234 = 43.5                   # in keV, specific gamma-ray energy for U-234 from
Pu-238
linewidth_u234 = 0.5                # in keV (adjusted for better visualization)

# Parameters for U-238 from Pu-242
activity_pu242_ci = 5.555e-6        # in curies (100 microCurie)
fraction_pu242 = 0.000384             # fraction of 44.9 keV gamma-ray emission
(0.0384%)
half_life_pu242 = 3.73e5 * 365.25 * 24 * 3600  # in seconds (373,000 years)
E_gamma_u238 = 44.7                   # in keV, specific gamma-ray energy for U-238 from
Pu-242
linewidth_u238 = 0.5                # in keV (adjusted for better visualization)

# Measurement time in seconds
measurement_time = 1 * 3600           # in seconds (1 hour)

# Detector parameters
num_channels = 100                  # number of channels for the histogram
energy_range = (39, 50)             # energy range in keV
resolution = 1                    # resolution of the detector in channel units

# Simulate energy distributions for U-234 and U-238
energies_u234 = simulate_gaussian_distribution(activity_pu238_ci, fraction_pu238,
half_life_pu238, measurement_time, E_gamma_u234, linewidth_u234)
energies_u238 = simulate_gaussian_distribution(activity_pu242_ci, fraction_pu242,
half_life_pu242, measurement_time, E_gamma_u238, linewidth_u238)
```

```
# Simulate detector response for U-234
hist_u234, bin_edges_u234 = simulate_detector_response(energies_u234, num_channels,
energy_range, resolution)

# Simulate detector response for U-238
hist_u238, bin_edges_u238 = simulate_detector_response(energies_u238, num_channels,
energy_range, resolution)

# Masks for low and high bands with single cutoff at 44.2 keV
cutoff_energy = 44.2
low_band_mask_u234 = bin_edges_u234[:-1] < cutoff_energy
high_band_mask_u234 = bin_edges_u234[:-1] >= cutoff_energy
low_band_mask_u238 = bin_edges_u238[:-1] < cutoff_energy
high_band_mask_u238 = bin_edges_u238[:-1] >= cutoff_energy

# Calculate total counts for U-234 and U-238
total_counts_u234 = np.sum(hist_u234)
total_counts_u238 = np.sum(hist_u238)

# Calculate counts in low and high bands for U-234 and U-238
counts_u234_low_band = np.sum(hist_u234[low_band_mask_u234])
counts_u234_high_band = np.sum(hist_u234[high_band_mask_u234])
counts_u238_low_band = np.sum(hist_u238[low_band_mask_u238])
counts_u238_high_band = np.sum(hist_u238[high_band_mask_u238])

# Calculate overlapping counts in the low and high bands
overlapping_counts_low_band =
np.sum(np.minimum(hist_u234[low_band_mask_u234],
hist_u238[low_band_mask_u238]))
overlapping_counts_high_band =
np.sum(np.minimum(hist_u234[high_band_mask_u234],
hist_u238[high_band_mask_u238]))

# Print the total counts and the counts in each band
print(f"Total counts for U-234: {total_counts_u234}")
print(f"Total counts for U-238: {total_counts_u238}")
print(f"Counts in the low band for U-234 (< {cutoff_energy} keV):
{counts_u234_low_band}")
print(f"Counts in the low band for U-238 (< {cutoff_energy} keV):
{counts_u238_low_band}")
print(f"Counts in the high band for U-234 (>= {cutoff_energy} keV):
{counts_u234_high_band}")
print(f"Counts in the high band for U-238 (>= {cutoff_energy} keV):
{counts_u238_high_band}")
print(f"Overlapping counts in the low band: {overlapping_counts_low_band}")
```

```
print(f"Overlapping counts in the high band: {overlapping_counts_high_band}")

# Plot detector response for both isotopes, showing full distribution
plt.figure(figsize=(12, 8))

# Plot U-234 full distribution
plt.bar(bin_edges_u234[:-1], hist_u234, width=np.diff(bin_edges_u234), color='blue',
alpha=0.3, label='U-234 from Pu-238 (Full Distribution)')

# Plot U-238 full distribution
plt.bar(bin_edges_u238[:-1], hist_u238, width=np.diff(bin_edges_u238), color='red',
alpha=0.3, label='U-238 from Pu-242 (Full Distribution)')

# Highlight low and high bands for U-234
plt.bar(bin_edges_u234[:-1][low_band_mask_u234], hist_u234[low_band_mask_u234],
width=np.diff(bin_edges_u234)[low_band_mask_u234], color='blue', alpha=0.6,
label='U-234 (Low Band)')
plt.bar(bin_edges_u234[:-1][high_band_mask_u234], hist_u234[high_band_mask_u234],
width=np.diff(bin_edges_u234)[high_band_mask_u234], color='cyan', alpha=0.6,
label='U-234 (High Band)')

# Highlight low and high bands for U-238
plt.bar(bin_edges_u238[:-1][low_band_mask_u238], hist_u238[low_band_mask_u238],
width=np.diff(bin_edges_u238)[low_band_mask_u238], color='red', alpha=0.6, label='U-
238 (Low Band)')
plt.bar(bin_edges_u238[:-1][high_band_mask_u238], hist_u238[high_band_mask_u238],
width=np.diff(bin_edges_u238)[high_band_mask_u238], color='orange', alpha=0.6,
label='U-238 (High Band)')

# Add vertical line at the cutoff energy (44.2 keV)
plt.axvline(cutoff_energy, color='black', linestyle='--', linewidth=1.5, label=f'Cutoff
Energy ({cutoff_energy} keV)')

plt.title('Detector Response for U-234 and U-238 with Single Cutoff Band Separation')
plt.xlabel('Energy (keV)')
plt.ylabel('Counts')
plt.grid()
plt.legend()

plt.tight_layout()
plt.show()

## -------------------- ##

import numpy as np
```

```
import matplotlib.pyplot as plt
from scipy.ndimage import gaussian_filter1d

# Constants
Avogadro = 6.022e23            # Avogadro's number
speed_of_light = 3.0e8         # speed of light in m/s

# Function to simulate Gaussian distribution of gamma-ray energies
def simulate_gaussian_distribution(activity_ci, fraction, half_life, measurement_time,
E_gamma, linewidth):
    activity = activity_ci * 3.7e10
    lambda_decay = np.log(2) / half_life
    N_decays = activity * measurement_time
    N_gamma = N_decays * fraction
    energies = np.random.normal(E_gamma, linewidth, int(N_gamma))
    return energies

# Function to simulate detector response with specified resolution
def simulate_detector_response(energies, num_channels, energy_range, resolution):
    hist, bin_edges = np.histogram(energies, bins=num_channels, range=energy_range,
density=False)
    smoothed_hist = gaussian_filter1d(hist, sigma=resolution)
    return smoothed_hist, bin_edges

# Parameters for U-234 from Pu-238
activity_pu238_ci = 0.0334e-6            # in curies (100 microCurie)
fraction_pu238 = 0.000392              # fraction of 43.5 keV gamma-ray emission
(0.0392%)
half_life_pu238 = 87.7 * 365.25 * 24 * 3600  # in seconds (87.7 years)
E_gamma_u234 = 43.5                    # in keV, specific gamma-ray energy for U-234 from
Pu-238
linewidth_u234 = 0.5                 # in keV (adjusted for better visualization)

# Parameters for U-238 from Pu-242
activity_pu242_ci = (95.9512e-6)*0.2             # in curies (100 microCurie)
fraction_pu242 = 0.000384              # fraction of 44.9 keV gamma-ray emission
(0.0384%)
half_life_pu242 = 3.73e5 * 365.25 * 24 * 3600  # in seconds (373,000 years)
E_gamma_u238 = 44.7                    # in keV, specific gamma-ray energy for U-238 from
Pu-242
linewidth_u238 = 0.5                 # in keV (adjusted for better visualization)

# Measurement time in seconds
measurement_time = 1 * 3600            # in seconds (1 hour)
```

```
# Detector parameters
num_channels = 100                  # number of channels for the histogram
energy_range = (39, 50)             # energy range in keV
resolution = 1                # resolution of the detector in channel units

# Simulate energy distributions for U-234 and U-238
energies_u234 = simulate_gaussian_distribution(activity_pu238_ci, fraction_pu238,
half_life_pu238, measurement_time, E_gamma_u234, linewidth_u234)
energies_u238 = simulate_gaussian_distribution(activity_pu242_ci, fraction_pu242,
half_life_pu242, measurement_time, E_gamma_u238, linewidth_u238)

# Simulate detector response for U-234
hist_u234, bin_edges_u234 = simulate_detector_response(energies_u234, num_channels,
energy_range, resolution)

# Simulate detector response for U-238
hist_u238, bin_edges_u238 = simulate_detector_response(energies_u238, num_channels,
energy_range, resolution)

# Masks for low and high bands with new thresholds at 43.5 keV and 44.7 keV
low_band_mask_u234 = bin_edges_u234[:-1] < 43.5
high_band_mask_u234 = bin_edges_u234[:-1] > 44.7
low_band_mask_u238 = bin_edges_u238[:-1] < 43.5
high_band_mask_u238 = bin_edges_u238[:-1] > 44.7

# Calculate total counts for U-234 and U-238
total_counts_u234 = np.sum(hist_u234)
total_counts_u238 = np.sum(hist_u238)

# Calculate counts in low and high bands for U-234 and U-238
counts_u234_low_band = np.sum(hist_u234[low_band_mask_u234])
counts_u234_high_band = np.sum(hist_u234[high_band_mask_u234])
counts_u238_low_band = np.sum(hist_u238[low_band_mask_u238])
counts_u238_high_band = np.sum(hist_u238[high_band_mask_u238])

# Calculate overlapping counts in the low and high bands
overlapping_counts_low_band =
np.sum(np.minimum(hist_u234[low_band_mask_u234],
hist_u238[low_band_mask_u238]))
overlapping_counts_high_band =
np.sum(np.minimum(hist_u234[high_band_mask_u234],
hist_u238[high_band_mask_u238]))

# Print the total counts and the counts in each band
print(f"Total counts for U-234: {total_counts_u234}")
```

```
print(f"Total counts for U-238: {total_counts_u238}")
print(f"Counts in the low band for U-234 (< 43.5 keV): {counts_u234_low_band}")
print(f"Counts in the low band for U-238 (< 43.5 keV): {counts_u238_low_band}")
print(f"Counts in the high band for U-234 (> 44.7 keV): {counts_u234_high_band}")
print(f"Counts in the high band for U-238 (> 44.7 keV): {counts_u238_high_band}")
print(f"Overlapping counts in the low band: {overlapping_counts_low_band}")
print(f"Overlapping counts in the high band: {overlapping_counts_high_band}")

# Plot detector response for both isotopes, showing full distribution
plt.figure(figsize=(12, 8))

# Plot U-234 full distribution
plt.bar(bin_edges_u234[:-1], hist_u234, width=np.diff(bin_edges_u234), color='blue',
alpha=0.3, label='U-234 from Pu-238 (Full Distribution)')

# Plot U-238 full distribution
plt.bar(bin_edges_u238[:-1], hist_u238, width=np.diff(bin_edges_u238), color='red',
alpha=0.3, label='U-238 from Pu-242 (Full Distribution)')

# Highlight low and high bands for U-234
plt.bar(bin_edges_u234[:-1][low_band_mask_u234], hist_u234[low_band_mask_u234],
width=np.diff(bin_edges_u234)[low_band_mask_u234], color='blue', alpha=0.6,
label='U-234 (Low Band)')
plt.bar(bin_edges_u234[:-1][high_band_mask_u234], hist_u234[high_band_mask_u234],
width=np.diff(bin_edges_u234)[high_band_mask_u234], color='cyan', alpha=0.6,
label='U-234 (High Band)')

# Highlight low and high bands for U-238
plt.bar(bin_edges_u238[:-1][low_band_mask_u238], hist_u238[low_band_mask_u238],
width=np.diff(bin_edges_u238)[low_band_mask_u238], color='red', alpha=0.6, label='U-
238 (Low Band)')
plt.bar(bin_edges_u238[:-1][high_band_mask_u238], hist_u238[high_band_mask_u238],
width=np.diff(bin_edges_u238)[high_band_mask_u238], color='orange', alpha=0.6,
label='U-238 (High Band)')

# Add vertical lines at 43.5 keV and 44.7 keV
plt.axvline(43.45, color='blue', linestyle='--', linewidth=1, label='Low Band Threshold
(43.5 keV)')
plt.axvline(44.7, color='red', linestyle='--', linewidth=1, label='High Band Threshold
(44.7 keV)')

plt.title('Detector Response for U-234 and U-238 with Full Distribution and Band
Highlights')
plt.xlabel('Energy (keV)')
plt.ylabel('Counts')
```

```
plt.grid()
plt.legend()

plt.tight_layout()
plt.show()
```